Tactile Sensing Using Elastomeric Sensors

by

Xiaodan (Stella) Jia

Submitted to the Department of Mechanical Engineering
in partial fulfillment of the requirements for the degree of

Master of Science in Mechanical Engineering

at the

MASSACHUSETTS INSTITUTE OF TECHNOLOGY

September 2012

Author .....
Department of Mechanical Engineering
Aug 16th, 2012

Certified by .....
Edward H. Adelson
John and Dorothy Wilson Professor
Thesis Supervisor

Certified by .....
Mandayam A. Srinivasan
Senior Research Scientist
Thesis Supervisor

Accepted by .....
David E. Hardt
Chairman, Department Committee on Graduate Theses

Tactile Sensing Using Elastomeric Sensors

by

Xiaodan (Stella) Jia

Submitted to the Department of Mechanical Engineering
on Aug 16th, 2012, in partial fulfillment of the
requirements for the degree of
Master of Science in Mechanical Engineering

Abstract

GelSight, namely, elastomeric sensor, is a novel tactile sensor to get the 3D information of contacting surfaces. Using GelSight, some tactile properties, such as softness and roughness, could be gained through image processing techniques. In this thesis, I implemented GelSight principle to reconstruct surface geometry of tested surfaces, based on which, the roughness comparison and lump detection experiment are conducted. Roughness of five different types of sandpapers are successfully compared using GelSight R_a value. In the lump detection experiment, a visual display for tactile information is presented. To get binary feedback of lump presence or not, a simple threshold method is introduced in this thesis. To evaluate the performance of GelSight sensor, human psychological experiments are conducted. In similar tasks, GelSight sensor outperforms humans in lump detection.

Thesis Supervisor: Edward H. Adelson
Title: John and Dorothy Wilson Professor

Thesis Supervisor: Mandayam A. Srinivasan
Title: Senior Research Scientist

Acknowledgments

GelSight sensor is really charming. Converting tactile information to an image display, GelSight could convey the tactile sensation more vividly comparing to other tactile sensors. This research project is so fascinating that I couldn't stop thinking about it even when I was dreaming. However, pushed by deadline is not fun. Thanks to prompt feedback from my advisors, Edward Adelson and Mandayam Srinivasan, I could make it at the last minute.

Prof. Adelson is a great scientist. He helps me with critical thinking and serious methods of data analysis. Dr. Srinivasan is a great engineer. He helps me with practical thinking and fundamental implementation. Without the help of these two helpful advisors, I couldn't make it here. I still remember the first time I hear about GelSight, I was so excited about it. Kimo Johnson is the one who introduced GelSight idea to me. He guided me at the very first beginning and built GelSight portable device, which is used in my lump detection experiment. I want to thank my boyfriend, Yida Zhang. We're having a long distance relationship. Since all my experiments should be done in the lab, I couldn't go and visit him. He devoted a lot of his time coming over to support me. Whenever I feel frustrated, he is always there to help me. Also, I want express my gratitude to my parents. I'm studying here in US, leaving them alone in the small town back in China. I don't have time to come back home and could't company them by the sides. They give all their love to me, which is the biggest support for me to stay in US by myself. They're the greatest parents in the world. My labmates, Rui Li, Bei Xiao, Krista Ehinger, Alvin Raj, Phillip Isola and Derya Akkaynak Yellin, are all very supportive whenever I need the help from them. John Canfield helped with all material supplies. Ron Wiken helps a lot for manufacturing the parts needed in my experiment setup. Toni Oliver helped with the payment for the supply needed for the phantom making.

Thank you all who've helped me in my research, my life and my thesis writing. I really appreciate every effort you spare to me.

Contents

List of Figures

List of Tables

Chapter 1

Introduction

GelSight, namely, elastomeric sensor, is a novel tactile sensor to get the 3D information of contacting surfaces. Using GelSight, some material properties, such as softness and roughness, could be detected through image processing techniques. In this thesis, I will introduce the basic idea of GelSight sensor and different types of GelSight devices. Experiments for roughness detection and lump detection using GelSight sensor are explained. The possibilities of softness detection and force feedback of GelSight sensor are discussed. Chapter one describes human tactile sensing system and existing robotic tactile sensors. Chapter two introduces the basic principles of GelSight sensor and key components of GelSight sensor. Previous GelSight devices are introduced. 3D reconstruction algorithm is explained and some results are shown in this chapter. Chapter three describes previous work in softness and roughness detection, and experiment of roughness comparision using GelSight sensor. Result of experiment for softness comparison of objects with same shape is shown. Chapter four shows application of tactile sensors in lumps detection using GelSight sensor. Human psychological experiment is conducted for doing similar task to compare the performance. Chapter five concludes the result of this research project and the work could be done in the future.

1.1 Definiation and Classification

Human rely on multiple sensory modalities to estimate environmental properties. Both, the eyes and the hands can provide information of objects and materials, but in contrast to vision, the hands are especially adapted to perceive material properties such as texture, temperature, and weight. Manual tactile perception is the ability to gather information about objects by using the hands [160]. The tactile properties of objects are processed by the somatosensory system, which uses information from receptors that respond to touch and vibration, body movement, temperature, and pain [91].

Baby's earliest explorations of himself and his environment are through his sense of touch ([159], [124]), his hands and mouth being the principle exploratory tools. [159] presented evidence for genuine tactile perception of material properties by infants as young as three months old, although they did not explore the objects with hand movements specific to the properties.

Most researchers have distinguished among three sensory systems, cutaneous, kinesthetic and haptic. According to Loomis and Lederman [115] and Klatzky and Lederman [98], a cutaneous system involves physical contact with the stimuli and provides awareness of the stimulation of the outer surface of boty by means of receptors in the skin and associated somatosensory area of central nervous system (CNS). The kinesthetic system provides information about the static and dynamic body postures (relative positioning of the head, torso, limbs, and end effectors) on the basis of afferent information from skin in kinesthetic sensing also indicates its dependence on cutaneous sensing. The haptic system uses significant information about objects and events both from cutaneous and kinesthetic system [115], [98].

The "sense of touch" in humans comprises two main submodalities, i.e., "cutaneous" and "kinesthetic", characterized on the basis of the site of sensory inputs. The cutaneous sense receives sensory inputs from the receptors embedded in the skin, and the kinesthetic sense receives sensory inputs from the receptors within muscles, tendons, and joints [115], [64]. It should be noted that sensory inputs are mechanical

stimulations but also heat, cooling, and various stimuli that produce pain. On the basis of sensory systems, the perception of a stimulus can be categorized as cutaneous, kinesthetic, and haptic perception. According to Loomis and Lederman [115], "tactile" perception refers to the perception mediated solely by variations in cutaneous stimulation. Linesthetic perception is mediated exclusively by the variations in kinesthetic stimulation. All perceptions mediated by cutaneous and/or kinesthetic sensibility are referred to as tactile perception. The properties of peripheral nervous system are investigated either with a moving object touching an observer or by the purposive exploration of objects by the observer. Accordingly, the "sense of touch" is classified as passive and active. Loomis and Lederman [115] made a distinction between passive and active touch by adding the motor control inputs to the afferent information. In an everyday context, the touch is active as the sensory apparatus is present on the body structures that produce movements [39].

Using various terms associated with the human "sense of touch", a parallel can be drawn for robotic tactile sensing. Generally, robotic tactile sensing is related to the measurements of forces in a predeterminded area. Jayawant [78] defined it as the continuous detection of forces in an array. Crowder [37] defined it as the detection and measurement of perpendicular forces in a predetermined area and subsequent interpretation of the spatial information. However, this definition is narrow for not including contact parameters other than perpendicular forces and broad for including the "interpretation" of spatial information, which is basically perception and, hence, includes the role of both cutaneous sensing and the corresponding area of analysis in somatosensory cortex of CNS. In this context, the definition of a tactile sensor, a device or system that can measure a given property of an object through contact in the world - by Lee and Nicholls [113] is more appropriate. Studies on cutaneous sensing show that receptors are not just transducers. Both individually and collectively they locally process the stimulus [81], [85], [20]. Thus, tactile sensing can be defined as detection and measurement of contact parameters in a predetermined contact area and subsequent preporcessing of the signals at the tactile level, i.e., before sending tactile data to higher levels for perceptual interpretation. On similar lines, touch

sensing can be termed as tactile sensing at single contact point [39].

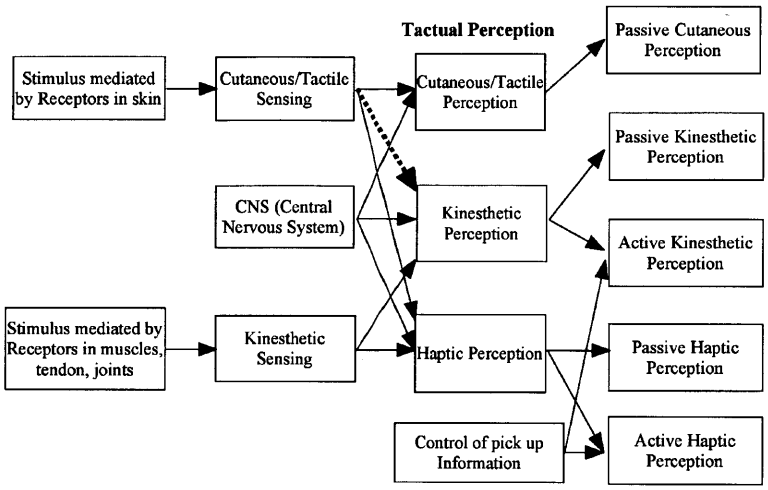

Figure 1-1: Componets of tactile perception [115]

Robotic tactile sensing is broadly classified in Figure 1-1. Based on the tasks to be accomplished, robotic tactile sensing is categorized in two ways, "perception for action" (as in grasp control, dexterous manipulation, etc.) and "action for perception" (as in object recognition, modeling, exploration, etc.). In addition to these, "haptics" could be the third category. Haptics involves both action and reaction, i.e., two-way transfer of touch information. Based on the body site, where tactile sensors are located, robotic tactile sensing can be categorized as intrinsic and extrinsic tactile sensing. Intrinsic sensors, which are placed within the mechanical structure of the robot, derive the contact information like magnitude of force using force sensors. Extrinsic sensors or arrays that are mounted at or near the contact interface deal with tactile data from localized regions. Extrinsic and intrinsic tactile sensing are analogous to cutaneous and kinesthetic sensing, respectively. Like a cutaneous system, extrinsic tactile sensing and the computational unit of robots can be termed as an extrinsic tactile sensing system. Similarly, an intrinsic tactile sensing system and haptic system can also be defined [39]. The extrinsic tactile sensing is further categorized in two ways, for highly sensitive parts (e.g., fingertips), and for less sensitive parts (e.g.,palm). Whereas former requires tactile sensing arrays with high density and spatiotemporal response $\sim 1mm$ spatial resolution and response time of the order of few

milliseconds), such constraints can be relaxed for the latter. The working principle of tactile sensors can be resistive, capacitive, inductive, optical, magnetic, piezoelectric, ultrasonic, magnetoelectric, etc [39]. Similarly, the physical nature of the sensors can be flexible, compliant, stiff and rigid, etc. This thesis is primarily focused on extrinsic tactile sensing, and thereafter, it is simply termed as tactile sensing.

1.2 Human Tactile Sensing System

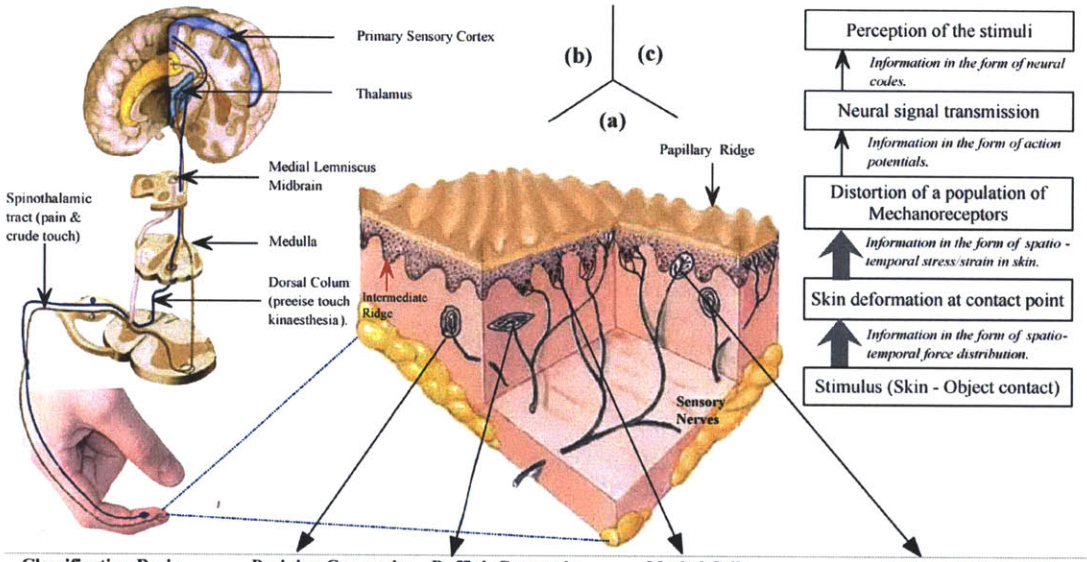

Classification Basis		Pacinian Corpuscle	Ruffini Corpuscle	Merkel Cells	Meissner's Corpuscle
Type		FA II	SA II	SA I	FA I
Adaptation Rate		Fast	Slow	Slow	Fast
Spatial Acuity (mm)		10+	7+	0.5	3-4
Vibration/rapid indent. threshold	Best(μm)	0.01	40	8	2
	Mean(μm)	0.08	300	30	6
Stimuli Frequency (Hz)		40-500+	100-500+	0.4-3	3-40
Conduction Velocity (m/s)		35-70	35-70	40-65	35-70
Effective Stimuli		Temporal changes in the skin deformation	Sustained downward Pressure; Lateral skin stretch; Skin slip.	Spatial deformation; Sustained pressure; Curvature, edge, corners.	Temporal changes in skin deformation
Sensory Function		High frequency vibration detection; Tool use.	Finger position; Stable grasp; Tangential Force; Motion direction	Pattern/form detection; texture perception; Tactile flow perception.	Low frequency vibration & motion detection; Grip control; Tactile flow perception.

Figure 1-2: Section of glabrous skin showing physical location and classification of various mechanoreceptors [169], [92], [135], [83], [165], [137]. (b) Tactile signal transmission, from fingertips to somatosensory area of brain (modified from [25]). (c) Functional events during tactile signal transmission from contact point to the brain. For simplicity, the signal flow is unidirectional. In general, the information transfer is bidirectional as the same path is used by motor signals. [39]

Human sense of touch deals with the spatiotemporal perception of external stimuli through a large number of receptors (e.g., mechanoreceptors for pressure/vibration, thermoreceptors for temperature, and nocioceptors for pain/ damage [84]) that are

distributed all over the body with variable density. the response to mechanical stimulus is mediated by mechanoreceptors that are embedded in the skin at different depths. The number, pre square centimeter area, is estimated to be 241 in the fingertips and 58 in the palm of adult humans [82]. The classification, functions, and location of these receptors are shown in Figure 1-2. They have different receptive fields, the extent of body area to which a receptor responds, and different rates of adaptation. A fast-adapting (FA) receptor responds with bursts of action potentials when its preferred stimulus is first applied and when it is removed. In contrast, a slow-adapting (SA) receptor remains active throughout the period during which the stimulus is in contact with its receptive field. SA-I mechanoreceptors exhibit fully tunable "stochastic resonance" [54], a process whereby a nonlinear system is able to detect an otherwise underectable signal (e.g., subthreshold stimulus) by adding a random stimulus or noise to the input.

The response to thermal stimulus is believe to be mediated by separated "warm" and "cold" thermoreceptor population in the skin. Nociceptor units in the skin are primarily responsible for sensation of pain; however, they also respond to extremes in temperature and sometimes to mechanical stimulation [98]. The nature of electrical discharge from various receptors in response to the external stimuli, studied in vitro and in vivo on human skin samples, is found to be pyroelectric and piezoelectric [9]. Comparative experiments on epidermis samples of skin show a marked phenomenological analogy with of piezoelectric materials [144].

1.2.1 Human Tactile Information Encoding

A variety of complex mechanical, perceptual, and cognitive phenomena take place the moment skin is stimulated until the perception. Figure 1-2 shows a sequence of events during tactile signal transfer. The skin conforms to its surface on contact with an object, maintains the same local contour, and thus projects the deformation to a large number of mechanoreceptors. Each mechanoreceptor represents a small portion of object and encodes the spatiotemporal tactile information as spikes of action potentials, voltage pulse generated when the stimulus is greater than the threshold.

The amplitude of the stimulus is then transformed to a train of action potentials [92], a step similar to digitizing and coding analog signals by an analog-to-digital (A/D) convertor [39].

The contact event related information is transmitted to CNS for higher level processing and interpretation via multiple nerves up to the spinal cord and via two major pathways: spinothalmaic and dorsal-column-medical-lemniscal (DCML), thereafter, as shown in Figure 1-2. The spinothalamic pathway is slower and carries temperature and pain related information. DCML, on other hand, quickly conveys pressure/vibration related information to the brain and helps in spatial and temporal comparisons of the stimuli. The tactile information is processed at various data transfer stages before it reaches the CNS. For example, during natural manipulations, humans can perceive independently the curvature and the direction of force from first spikes of the ensembles of primary sensory neurons in the terminal phalanx [81], [85]. This reduces the computational burden of CNS and let it perform some higher level processing like disentangling the interactions between information obtained from ensemble of first spikes and other parameters like rate of change of contact force, temperature, change in viscoelastic properties of the fingertip, etc. [79]. The tactile information transfer to brain is also subjected to an intense process of selection [17].

1.2.2 Human Tactile Sensitivities

Spatiotemporal limits and sensitivity to mechanical stimulus directly affect the object recognition capability [115] and directional sensitivity [166], etc. The pattern sensing capability of the cutaneous sense is limited by both its spatial and temporal sensitivities, as they quantify the information loss or blurring of stimulus by spatiotemporal filtering at early stage of cutaneous processing [115].

Spatial acuity is an important parameter that gives an idea of spatial resolution, the smallest separation at which one can tell if he/she has been touched at two points. Two points threshold [80] and grating orientation method [32] show that the spatial acuity varies across the body, from highest at fingertips, face, toes, etc., to lowest

at thigh, belly, etc. The spatial resolution at the palm is about seven times smaller than that at the fingertips [35]. One can resolve two points as close as $1mm$ on the fingertips [34] and up to 30 mm on the belly [169]. Besides body site, the ability to perceive a fine spatial structure also depends on the temporal properties of stimulus (namely, its vibration frequency). The spatial acuity decreases if vibratory frequency is increased [15]. The spatial acuity in the torso, measured with vibrotactile stimuli, has been reported to be $20 \sim 30mm$ [53]. Skin microstructures like intermediate ridges, the undulating epidermal tissues that descend into the epidermal, dermal junction (shown in figure 1-2), also enhance the tactile spatial acuity by transmitting magnified signals from surface of skin to the mechanoreceptors [108], [39].

When it comes to temporal resolution, humans are capable of detecting vibrations up to 700 Hz, i.e., they can detect a single temporal interval of about 1.4 ms [98]. Temporal separation of two contact events, at different locations, is also needed as it helps in detecting the presence of multiple events. The critical temporal separation for two events at different locations on fingertips is found to be on the order of $30 \sim 50ms$ [33]. The pressure threshold and skin deformation are other common intensive measures of absolute tactile sensitivity.

The higher the pressure threshold, the lower the sensitivity of the body part. Controlled pressure sensitive studies show that pressure thresholds vary with body site. Whereas normal mean threshold values average about 0.158 g on the palm and about 0.055 g on the fingertips of men, the corresponding values for women are 0.032 g and 0.019 g, respectively, [89].

The temperature sensitivity also varies with the body parts. For example, from a baseline temperature of 33°C, changes as small as 0.16 and 0.12°C for warmth and cold, respectively, can be detected at the fingertips [158]. Corresponding values at volar base of thumb are 0.11 and 0.07°C.

1.2.3 Human Tactile Perception

Humans are excellent at recognizing common objects by touch alone [99], and cues like material properties, shape, etc., are critical to this endeavor. Both cutaneous and

kinesthetic sensing contribute to the perception of such cues.

Tactile sensing in humans is better adapted to feel material properties of objects than to feel their shapes. Shape detection of objects small enough to be within the contact area ($7 \sim 12mm$) of the fingertips is an important function of the mechanoreceptors. Experiments involving vertical indentation and stroking of skin, with the force equal to that exerted by humans during natural manipulation (1590 g wt.), indicate that the object shape and orientation are signaled by the spatiotemporal responses of the afferent fiber populations, particularly those of the SAs [107] [60] [93]. The curvature and force direction can also be perceived from these signals [79]. These experiments reveal that the firing rate of an SA is a function of the vertical displacement, vertical velocity, and the amount and the rate of change of curvature of the skin. However, SAs become silent in the event of negative rate of change of curvature. In the case of FA, the firing rate is a function of the vertical velocity and the rate of change of curvature at the most sensitive part of the receptive field. These studies give a direct relation between the stimuli and neural signals that code them. Thus, assuming skin to be a "blackbox, the relation between the stimuli (e.g., the shape) and the output (e.g., the firing rate) of afferent fibers can be written as below:

$$f_{SA} = a_1 R^{-1} + a_2 \frac{dR^{-1}}{dt} + a_3 \Delta Z + a_4 \frac{dZ}{dt} \tag{1.1}$$

$$f_{FA} = b_2 \frac{dR^{-1}}{dt} + b_4 \frac{dZ}{dt} \tag{1.2}$$

where f_{SA} and f_{FA} are the firing rates of SA and FA receptors, respectively, R^{-1} is the skin curvature at contact point, ΔZ is the vertical displacement, and a_1, a_2, a_3, a_4, b_2 and b_4 are the constants. The equations above is from Srinivasan's paper in [141]. The edge sensitivity is a special case of sensitivity to changes in skin curvatures. As can be noticed from (1.1) and (1.2), FA and SA receptors respond simultaneously at edges and boundaries, and at other points, FA receptors are silent. The response of SA receptors is higher at edges than at a uniform surface because of high compressive strain at such points. The edge detection sensitivity of SA I receptors has also been attributed to the presence of Merkel cells on the tips of the epidermal part of

intermediate ridges. Intermediate ridges are believed to magnify the tactile signals from the surface of the skin to the mechanoreceptors by way of microlever action [23], [110]. The role of intermediate ridges studied through continuum mechanics or finite element modeling also show that the concentration of stress on the ridge tips improves the capability to differentiate finer details [58]. Surprisingly, the mechanoreceptors are located close to the points where stress is concentrated. Sensitivity of receptors to the rate of change of curvature, in addition to the curvature, also enhances the contrast at the edges of objects, where curvature changes abruptly.

Roughness-smoothness is another important perceptual dimension. Neurophysiological studies suggest that the tactile roughness perception is accurately predicted by spatial variations of discharge of SA afferents, and hence, it is a function of multiple tactile elements. Contrary to the general belief that the temporal parameters have little effect on roughness perception [122], recent studies show that they indeed contribute [22]. Fingerprints or papillary ridges, shown in Figure 1-2, also enhance the tactile sensitivity of Pacinian corpuscles and, hence, help in feeling fine textures [147]. Discrimination of surface roughness is also enhanced when tangential movement exists between the surface and skin [125], and this is independent of the mode (active or passive) of touch [109]. Roughness of objects is significantly correlated with friction as well. The correlation is much stronger when the variations and rate of change of the tangential forces are considered. This is evident from the experiments where subjects maintained a steady normal force, rather than reducing it, to allow the tangential force to initiate and maintain sliding while scanning a surface with higher friction [152], [153]. These facts point towards the importance of tangential force and that its knowledge, in addition to the normal forces, can be useful for robotic applications.

Detection of slip can be viewed as the coding of motion by the receptors in the skin. Slip or relative movement between a surface and the skin is important for perception of roughness [122], [152], [86], hardness [157], and shape [19], [177]. Slip plays an important role in grip force control by acting as an error signal. All these, except static contact associated with thermal sensing, involve finger movements and thus highlight the importance of dynamic tactile sensing [72].

Tactile feedback from the contact surface of an object influences the perception of force used to support it. Experiments studying the effect of tactile sensing on the perception of force demonstrate underestimation of forces produced by muscles when tactile sensory feedback from hand is constrained [90]. Interestingly, complete elimination of tactile feedback by anesthetizing skin results in an opposite perception of force, i.e., increase in the perceived force or heaviness [95] and decrease in the maximum force that the fingers can produce [10]. Further, the effect of eliminating the tactile sensing from various fingers is also different. Elimination of cutaneous sensing from thumb and index finger results in an increase of perceived heaviness by 40% and 13%, respectively [95]. In addition to magnitude, the direction of force is also critical for handling objects with irregular shapes while maintaining the desired orientation. Tactile afferents from the terminal phalanx of finger contribute to the encoding of direction of fingertip forces. The directionality is also thought to be due to different strains produced at the receptor site by forces applied in different directions [19].

However, human system is a complete, multilevel, integrated system, and the "sense of touch is not isolated. Multiple sensory information from several sensory modalities like touch, vision, hearing, etc., is needed to perceive a stimulus [92]. Sometimes, the sensory modalities compete (e.g., in presence of attention), and at other times, the whole is an integrated combination of the different sensory inputs. Even if a single modality is involved, the perception of an object can be due to a combined contribution of its sub modalities. The combination and integration of sensory information from multiple sources is key to robust perception, as it maximizes the information derived from the different sensory modalities and improves the reliability of the sensory estimate. Both vision and proprioception provide information about the position of the hand in space [13]. Haptically and visually acquired size-related information may influence the feed-forward or anticipatory control of forces during loading and transitional phases of precision grip [62], [61].

1.2.4 Skin Mechanics and Tactile Sensing

Skin acts as a medium through which contact indentations are converted into stresses/ strains. Human skin is multilayered, nonlinear, nonhomogeneous, and viscoelastic. It is a complex structure supported on a deformable system of muscles and fat [110]. Various skin layers have different stiffness. The base epidermis layer, having Youngs modulus 1010,000 times that of dermis, is considerably stiffer than the dermis [58]. With such properties, the skin mechanics is bound to play an important role in the tactile perception. The presence of physical interlocking between the epidermis and dermis layers of skin helps in resisting any tendency of their relative sliding over each other and creates a filtering mechanism that distributes forces and stresses from their point of application [139]. Such a filtering mechanism also has considerable impact on the spatial resolution. The presence of intermediate ridges and their role in magnifying the tactile signals by way of microlever action has already been discussed. Intermediate ridges, which are shown in Figure 1-2, should not be confused with papillary ridges or fingerprints that are basically the external parallel whorls. However, the center of each papillary ridge protuberance lies directly above the center of each intermediate ridge [58]. Papillary ridges are known to improve gripping [118] and tactile acuity by microlever mechanism [23], [110]. However, finite element studies indicate very little involvement of papillary ridges in such a mechanism [59]. Fingerprints might improve the tactile sensitivity of pacinian corpuscles and, hence, help us feel fine texture [147]. A number of attempts have been made to model and study the mechanical behaviors of the skin [135], [58], [42], [59].

1.3 Current Robotic Tactile Sensors

Tactile information is useful in robotics in a number of ways. In manipulative tasks, tactile information is used as a control parameter [114], [71], [16], and the required information typically includes contact point estimation, surface normal and curvature measurement, and slip detection [55] through measurement of normal static forces. A measure of the contact forces allows grasp force control, which is essential for

maintaining stable grasps [18]. The grasp force along with manipulator displacement is also needed in compliant manipulators [38]. In addition to magnitude, the direction of force is also critical, in dexterous manipulation, to regulate the balance between normal and tangential forces, and hence to ensure grasp stability the so-called friction cone [126]. For full grasp force and torque determination, shear information is also required [50], [143]. The need for shear stress information is also supported by finite element analysis (FEA) [142], [52]. Shear information is useful to determine the coefficient of friction and in getting a unique surface stress profile when the sensor is covered with elastomeric layer [129]. Importance of shear force in humans has already been discussed. While interacting with objects, a significant information such as shape [56], [146], [24], surface texture [120], [36], slip [36], [70], [11], [164], etc., comes through normal and shear forces.

However, a real-world interaction, involving both manipulation and exploration, also requires measuring material properties such as hardness [150], temperature [174], etc. Taxels based on design hints can possibly help in achieving some of the above objectives. Some of these design guidelines have been explored and tactile sensors exist with variable stiffness elastic layers [68], finger print like structures [172], and the mechanical properties and distributed touch receptors like human skin [168]. However, their number and the type of contact parameters obtained from them are still insufficient. For example, the interaction of robots with environment through tactile sensing has largely been limited to the measurement of static interaction forces, whereas real world interaction involves both static and dynamic. Similarly, most of the sensors are designed to measure static pressure or forces, from which, it is difficult to obtain information like stickiness, texture, hardness, elasticity, etc. Recently, the importance of dynamic events has been recognized, and sensors are being developed for detecting stress changes [148], [72], incipient slip [172], strain changes [94], and other temporal contact events. A range of sensors that can detect object shape, size, position, forces, and temperature have been reported in [69], [113], [45], [145]. Few exam- ples of sensors that could detect surface texture [120], [36], hardness or consistency [132], [150], and friction [117] are also described in the literature. Very few

examples of sensors that can detect force as well its direction have been reported [28], [163].

Advanced robotic systems require multimodal sensory information to interact safely, to make decisions, and to successfully carry out actions, all in an autonomous way. Sensor based robotic interaction has generally been investigated using vision and auditory sensors. However, the information obtained with visual and auditory sensors can sometimes be misleading due to the lack of contact information. The rich interaction behaviors exhibited by real world objects also depend on how heavy and stiff the contacted objects are, how their surfaces feel when touched, how they deform on contact, and how they move when pushed, etc. Therefore, using the tactile data along with that coming from existing sensory apparatus will greatly enhance the real world model generation capability of robots [39].

Over the past two decades or so, the pursuit to improve tactile sense capability of robots has resulted in many touch sensors, exploring nearly all modes of transductions. The tactile sensors used on robotics fall into several categories.

1.3.1 Resistive Sensors

Tactile sensors based on resistive mode of transduction have resistance values depending on the contact location and the applied force or, in other words, piezoresistance. Resistive touch sensors are generally sensitive and economic but consume lot of power. Their other limitation is that they measure only one contact location. An improved design using parallel analog resistive sensing strips, which is reported in [175], allows measuring many contact points. However, the lack of contact force measurement still remains a critical problem.

Piezoresistive touch sensors are made of materials whose resistance changes with force/pressure. The touch sensing system using this mode has been used in anthropomorphic hands [167]. Piezoresistive tactile sensing is particularly popular among microelectromechanical systems (MEMS) and silicon (Si)-based tactile sensors [12], [170]. The force-sensing resistor (FSR), which is widely used in pointing and position sensing devices such as joysticks, are also based on piezoresistive sensing technology.

Commercially available from Interlink [51], they have been used in many experimental tactile systems and advanced robotic hands [49]. FSRs are appealing, because of low cost, good sensitivity, low noise, and simple electronics. However, the requirement of serial or manual assembly, relatively stiff backing, nonlinear response, and large hysteresis are some of the drawbacks of FSRs.

1.3.2 Tunnel Effect Tactile Sensors

Tactile sensors based on quantum tunnel composites (QTC) have come up recently. Commercially available from Peratech [134], QTC has the unique capability of transforming from a virtually perfect insulator to a metal like conductor when deformed by compressing, twisting, or stretching. In QTC, the metal particles never come into contact; instead, they get so close that quantum tunneling (of electrons) takes place between the metal particles. Robotic hands with QTC-based taxels have been reported in [31] and [30]. A highly sensitive sensor based on electron tunneling principle is also reported in [120]. The device directly converts stress into electroluminescent light and modulates local current density, both being linearly proportional to local stress. With thin film, having metal and semiconducting nanoparticles, the sensor is $2.5cm^2$ in size and attains a spatial resolution of $40m$ far better than that of human fingertips. However, using charge- coupled device (CCD) camera, in current form, adds to the sensor size and makes its integration difficult on the robot.

1.3.3 Capacitive Sensors

Capacitive taxels have been widely used in robotics [63], [148], [123]. They can be made very small, which allows the construction of dense sensor arrays. An array of capacitive sensors which couples to the object by means of little brushes of fibers is reported in [148]. The sensor elements on the array are reportedly very sensitive (with a threshold of about 5 mN) and robust enough to withstand forces during grasping. An 8×8 capacitive tactile sensing array with $1mm^2$ area and spatial resolution at least ten times better than humans is reported in [63]. Capacitive sensing is also

popular among the tactile sensors based on MEMS and Si micromachining [29], [63], [46], [148]. Commercially available touch sensors such as RoboTouch and DigiTacts from pressure profile systems [75] and iPod-touch [8] are all based on capacitive technology. Availability of commercial capacitance to digital convertor chip like AD7147: CapTouch from Analog Devices [48] has made it easier to design thin and reliable contemporary touch controls for sensors that use capacitive technology. The utility of such a chip in getting the digitized data corresponding to change in capacitance at the contact point has been demonstrated in [119]. Touch sensors based on capacitive mode of transduction are very sensitive, but stray capacity and severe hysteresis are major drawbacks.

1.3.4 Optical Sensors

Tactile sensors with optical mode of transduction use the change in light intensity, at media of different refractive indices, to measure the pressure. Optical fiberbased taxel capable of measuring normal forces is reported in [67]. The sensor can measure forces as low as 1 mN with the spatial resolution of 5 mm. An optical three axial taxel capable of measuring normal and shear forces is reported in [130]. Some cases of large area skin based on LEDs have been reported in [131] and [26] as well. Commercial taxels using optical mode of transduction are also available, e.g., "KINOTEX [140]. Optical-based taxels are immune to electromagnetic interference, are flexible, sensitive, and fast but at times they are bulky. For example, even after miniaturization, the optical taxel reported in [116] has diameter 32 mm, length 60 mm, and a weight of 100 g. Loss of light by microbending and chirping, which cause distortion in the signal, are some other issues associated with optical sensors.

1.3.5 Ultrasonics-Based Sensors

Acoustic ultrasonics is another technology used for developing tactile sensors. The microphones, based on ultrasonics, have been used to detect surface noise occurring at the onset of motion and during slip. A 2×2 tactile array of polyvinylidene

fluoride (PVDF), which is described in [7], senses contact events from their ultrasonic emission at the contact point. Here, PVDF polymer is used as receiver to localize the contact point on a silicone rubber-sensing dome. The sensor is reportedly very effective in detecting slip and surface roughness during movement. Another simple and elastic tactile sensor, utilizing acoustic resonance frequency, to detect contact parameters like principal stress, friction, and slip is described in [151] and [127]. The resonant frequency of piezoelectric materials changes when they come in contact with the objects having different acoustic impedances [41], [40]. This property has been utilized to detect hardness and/or softness [132] and force/pressure [103]. Ultrasonic-based taxels have fast dynamic response and good force resolution. However, many such sensors use materials like lead zirconate titanate (PZT), which are difficult to process in miniaturized circuits. Using piezoelectric polymers can greatly simply such difficulties.

1.3.6 Magnetism-Based Sensors

Such tactile sensors measure the change in flux density as a result of the applied force. The flux measurement can be made either by Hall effect device [163], [77] or a magnetoresistive device [128]. The taxels based on magnetic principle have a number of advantages that include high sensitivity, good dynamic range, no measurable mechanical hysteresis, a linear response, and physical robustness. However, their usage is limited to nonmagnetic mediums.

1.3.7 Piezoelectric Sensors

The piezoelectric materials generate charge in proportion to the applied force/pressure. Piezoelectric materials like PZT, PVDF, etc., are suitable for dynamic tactile sensing. Though quartz and ceramics (e.g., PZT) have better piezoelectric properties; the polymers such as PVDF are preferred in touch sensors due to their excellent features like flexibility, workability, and chemical stability [57]. The use of PVDF for tactile sensing was reported for first time in [45], and thereafter, a number of works based

on PVDF or its copolymers have been reported in [102], [174], and [101], [172], [43], [27]. Temperature sensitivity of piezoelectric materials is a major cause of concern.

Production of tactile sensors with innovative designs still continues, but they largely remain unsatisfactory for robotics either because they are too big to be used without sacrificing dexterity or because they are slow, fragile, lack elasticity, lack mechanical flexibility, and lack robustness, and in some cases, because of their digital nature, i.e., all or none. Some other reasons for neglecting tactile sensing in a general mechatronic systems are discussed in [112].

Chapter 2

Principles and Devices of Elastomeric Sensor - GelSight

GelSight sensor is a novel tactile sensor that can be used to capture the surface geometry. GelSight sensor consists of a piece of clear elastomer coated with a reflective membrane. When the object pressed on the membrane, the membrane distorts to take on the shape of the object's surface. When viewed from behind (through the elastomer piece), the membrane appears as a relief replica of the surface. A camera records an image of this relief, using illumination from LEDs located in different directions. Using photometric stereo algorithm, the surface geometry could be reconstructed. GelSight sensor could also deal with transparent or specular materials because the membrane supplies its own BRDF [87]. The sensor uses inexpensive materials, and has the ability to obtain 2 microns resolution, and also can be made into a portable device that can be used "in the field" to record surface shape and texture [87]. We refer the sensor as "GelSight" sensor because it means to give you a sight through the gel.

2.1 Basic Principles of Elastomeric Sensor

Figure 2-1 shows the basic principle of GelSight. LEDs illuminate the surface of the gel, and the camera in the back of the supporting plate to takes the picture of

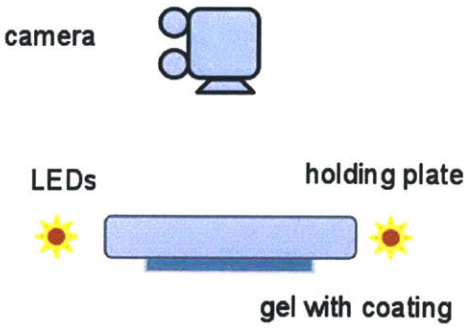

Figure 2-1: Basic principle of Gelsight sensor

the contacting surfaces. With images under illumination from different directions, photometric stereo algorithm is applied to get the depth information, and thus to reconstruct the surface geometry of tested surface. Figure 2-2a and 2-2b shows an Oreo cookie being pressed against the GelSight sensor. The reflective membrane, which is made from opaque elastomer paint, takes on the shape of the Oreos surface. Oblique illumination converts the deformation to a shaded image. The reflective membrane, which is made from opaque elastomer paint, takes on the shape of the Oreos surface [87].

(a) (b) (c)

Figure 2-2: (a) A cookie is pressed against the membrane of GelSight sensor. (b) The membrane is distorted, as shown in this view from beneath. (c) The cookies shape can be measured using photometric stereo and rendered at a different viewpoint. [87]

2.2 Components of GelSight Sensor

Even though GelSight idea is simple in concept, the performance of the GelSight sensor depends heavily on the construction of the sensor membrane, the elastomer

used for the sensor itself, the illumination design and the reconstruction algorithm. There are four main components for GelSight sensor: elastomer with the opaque reflective membrane on top of it, supporting plate which provides the support of the soft elastomer while pushing against the object, optics and LEDs which provide illumination for the sensor, and the camera in the back to capture the deformation images under the illumination from different directions. Sometimes, the optics could functions as a supporting plate as well.

2.2.1 Gel and Coating

The choice of elastomer comes first. In [87], Johnson mentioned the polymers used in their experiment, including silicones, polyurethanes, and thermoplastic elastomers (TPEs) such as styrene block copolymers. TPEs is the most commonly used material in Johnson's experiment, because they combine elasticity and strength. TPEs can be formed into arbitrary shapes and are fairly robust, returning to their original shape under normal usage.

Both of the pigment and the method of application determine the BRDF of the membrane. As mentioned in [87], diffuse BRDFs are useful for measuring relatively deep objects (depths on the order of 1 cm) and specular BRDF is good for capturing small variations in the surface normal. An ordinary pigment (such as titanium dioxide) yields a diffuse BRDF, while fine metal flakes (usually aluminum or bronze) produce specular BRDF. The choice between diffuse or specular BRDFs is a tradeoff between depth and detail.

The thickness of the elastomer determines the maximum depth variation that can be measured. Johnson did experiment of sensors with thicknesses ranging from less than 1 mm to 4 cm in [87]. The hardness of the elastomer used for GelSight sensor are Shore A 5 $\approx$ 20. (Elastomer is commonly measured on the Shore A scale, where 5 is very soft and 95 is very hard.)

The size and shape of the pigment used for the membrane impose a huge effect on the resolution of the system. In Figure 2-3, both images show Washingtons nose on a US quarter. The pigment used in 2-3 (a) is metal-flake, which visible in the image.

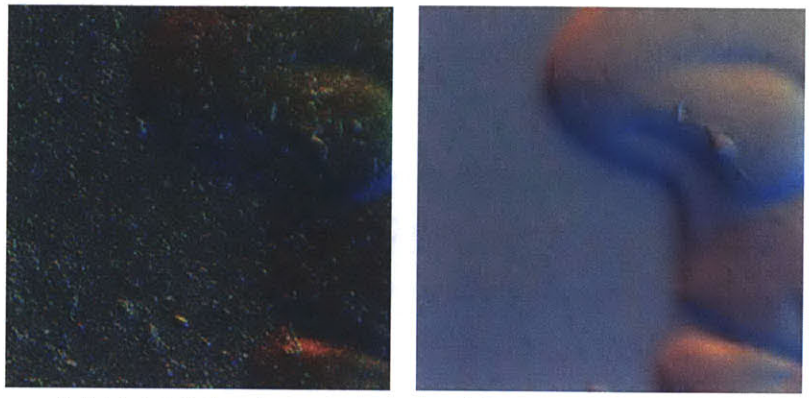

(a) Metal-flake pigment (b) Silver-powder pigment

Figure 2-3: GelSight sensor with different membrane for measuring the same surface [88]

These effects will cause noise in the estimated surface. The pigment used in 2-3 (b) is silver powder, the average size of which is below 1 micron. The near-spherical shape reduces noise due to random particle orientation [88]. The resolution of the sensor also depends on the rigidity of the elastomer. [87] uses 3M VHB mounting tape and achieved high-resolution results for hard surfaces in the bench setting.

2.2.2 Illumination

In addition to the elastomer, the illumination matters a lot for further reconstruction algorithms to obtain fine surface geometry. LEDs are the light source to use in all the settings, since it's cheap, small, power-saver. Also, some LEDs are directional, and under some circumstances, this will help with the illumination conditions.

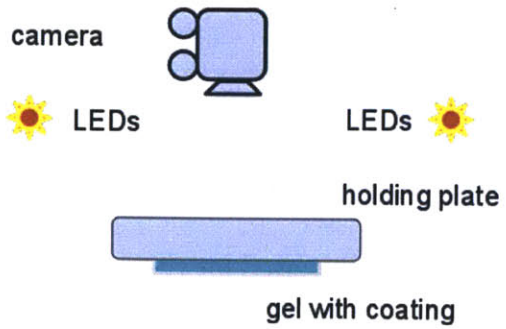

Figure 2-4: Basic principle of GelSight sensor

The condition to reconstruct the surface geometry is to have the illumination uniform across the sensor contacting surfaces, which will get rid of the location factor. As shown in Figure 2-4, the lights are upper high to roughly 30° and 8 inches away from the supporting plate. The distance from the lights to the illuminated surface should be ten times the length of the illuminated area, in which case the lights are regarded as distant lighting. The box setting, which will be introduced in the following section, takes this type of illumination. The advantage of this illumination type is that the lights are far away from the sensor, which could be regarded as the distant light source with parallel light rays. For the images captured from the camera, all the positions on the sensor could receive equal illumination, which could provide a great image quality for further reconstruction approaches. However, the disadvantage is that the device will be huge to hold the lights inside of it.

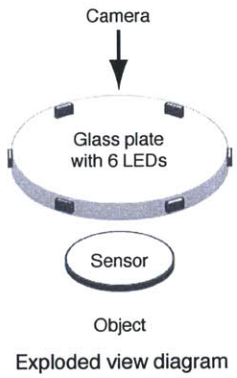

Figure 2-5: New lighting configuration to create grazing illumination across the sensor. [88]

For a diffuse surface, contrast is maximized under grazing illumination. As shown in [88], Johnson set up a new lighting configuration is introduced to create grazing illumination across the sensor. As in figure 2-5, six surface-mount LEDs are spaced equally around the edge of a glass disc. The glass disc is used as a mounting plate for the elastomeric sensor and the light from the LEDs propagates within the disc by total internal reflection. Each LED provides a different lighting condition for photometric stereo. This illumination design dramatically increases contrast, as shown in Figure **??**. In the portable setting and the bench setting to measure the fine details of

the surfaces, Johnson use this type of illumination condition. The advantage of this illumination method is that even though there are shadow areas in each image, there are six images in total to compensate the loss. And the device could be more compact comparing to the illumination in Figure 2-4.

2.2.3 Camera

Camera is another key component for building up the GelSight sensor. The quality of the camera will directly influence the resolution of the images. Canon digital SLR (EOS-1D Mark III) equipped with a 100 mm macro lens, is the first one used for the GelSight device in [87]. In [88], 0.8-megapixel Point Grey Flea2 firewire camera (1032 776 pixels) is used in the portable device to capture the surface geometry in the wild. 18-megapixel Canon EOS Rebel T2i camera with a Canon MP-E 65 mm macro lens, is used for the bench setting in [88] to capture the microgeometry.

2.3 GelSight Sensor Devices

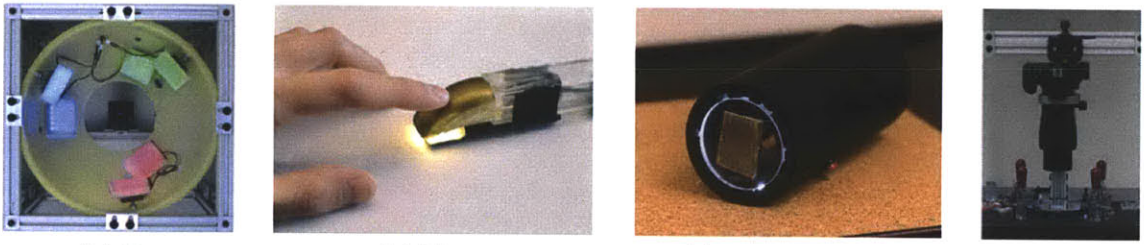

(a) Box (b) Finger (c) Portable device (d) Bench

Figure 2-6: (a) shows the box setting the first time GelSight is invented [87]. (b) shows the finger shape setup with GelSight idea. (c) shows the portable device to measure surfaces in the field [88]. (d) shows the bench setting in 2011 for the precise surface geometry measurement [88].

The principle of GelSight sensor is simple, however, to have a usable device is not that easy. As discussed earlier, all small components matter a lot for the final result. Figure 2-6 shows all the GelSight devices in the past.

2.3.1 Box Setting

Figure 2-7a is the first device for GelSight sensor. As shown in Figure 2-7, the device is within a 20 by 20 by 20 inches cubic box. Inside of the box, a camera is mounted aiming straight at the sensor from a distance of 16 inches. The camera used for Johnson and Adelson's result in [87] is by a Canon digital SLR (EOS-1D Mark III) equipped with a 100 mm macro lens. In the box, there are red, green, and blue floodlights that utilize LED arrays, positioned 10 inches away from the center of the sensor at an elevation angle of 30 degrees.

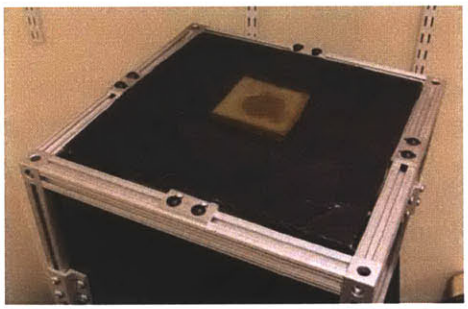

(a) Box top view

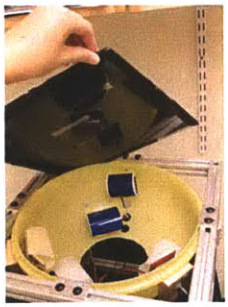

(b) Box inside view

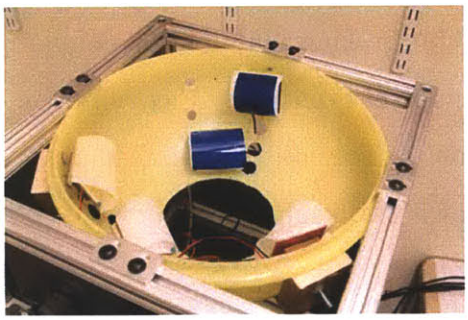

(c) Lights

(d) Camera

Figure 2-7: (a) shows the outlook of box setting. (b) shows inside view of the box setting. (c) shows the lights configuration in the box setting. (d) shows camera position related to the sensor in the box setting

Figure 2-8 shows a decorative pin (a) and the RGB image (b) that is captured when the object is pressed against the sensor from behind and (c) shows rendering of estimated surface. For traditional techniques (including photometric stereo), the pin is a challenging object, because it has a transparent glass-like material in the center surrounded by gold-plated metal.

(a) (b) (c)

Figure 2-8: (a) This decorative pin consists of a glass portrait mounted in a shiny gold setting. (b) The RGB image provided by the retrographic sensor. The pin is pressed into the elastomer skin, and colored lights illuminate it from three directions. (c) Rendering of the decorative pin [87]

2.3.2 Portable Setting

The Portable device (as shown in Figure 2-7c and Figure 2-9) is constructed from an acrylic tube with 3 inch outside diameter. The tube is approximately 8 inches long. The sensor is mounted on the exterior of a 0.25 inch thick, 2.25 inch diameter glass plate at one end of the tube. Our grazing illumination configuration leaves the interior of the tube free for a 0.8-megapixel Point Grey Flea2 firewire camera (1032 $\times$ 776 pixels). When an exterior button is pressed, the system rapidly captures the six lighting conditions. Figure 2-10 shows the result using portable deviece to measure the board and brick in the field.

(a) (b)

Figure 2-9: Portable setting for measuring surface geometry in the field [88]

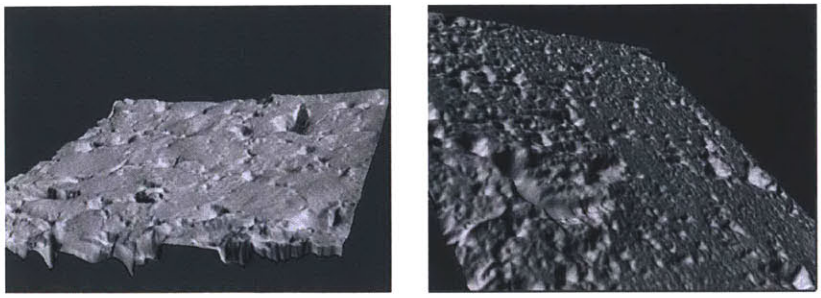

(a) (b)

Figure 2-10: Result of the measurement for Figure 2-9 [88]

2.3.3 Bench Setting

The bench setting (as shown in Figure 2-7d) consists of a 18-megapixel Canon EOS Rebel T2i camera with a Canon MP-E 65 mm macro lens mounted vertically over an optical bench. The elastomeric sensor is mounted on a 0.5-inch thick, 5.5-inch diameter glass plate with six LEDs evenly spaced around the perimeter. The glass plate and sensor are secured to the subject material with toggle clamps.

The bench setting is designed to measure microgeometry. Figure 2-11 shows the measurement of the letter T of the word Treasure on $ 20 bill. You can see both the rays painting and the fibers of the bill. Currently, we could resolve features as small as 2 microns spatially with sub-micron depth resolution.

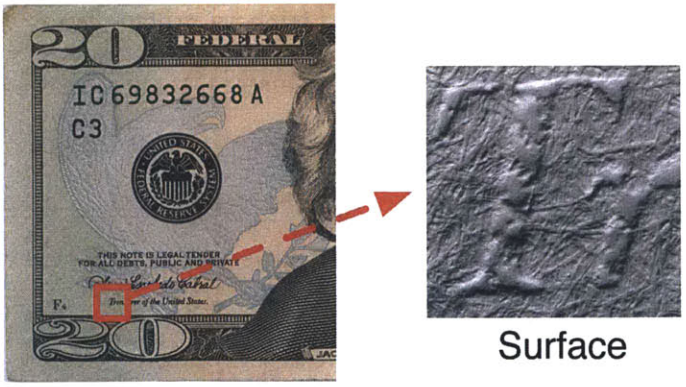

Figure 2-11: $ 20 bill is pressed into GelSight sensor. The details of bill fiber could be measured clearly. [88]

2.4 3D Reconstruction Method

In order to extract the shape from a set of images, Johnson and Adelson [87] apply a photometric stereo algorithm tailored to the sensor. They could reconstruct the surface, rendered in Figure 2-2c. Here some basic idea of 3D reconstruction using photometric stereo algorithm is explained. For more detailed information, please refer to [87] and [88].

2.4.1 Reconstruction Algorithm

The surface of elatomeric sensor is modeled with a height function $z = f(x, y)$. The height function represents the displacement of the sensor from its resting state; when nothing is touching the sensor, the height is zero. Assuming that image projection is orthographic, the position (x, y) in the image corresponds to the location (x, y) on the sensor. Under this assumption, the gradient (p, q) at position (x, y) is given by

$$p = \frac{\delta f}{\delta x}, q = \frac{\delta f}{\delta y} \tag{2.1}$$

and the surface normal is $N(x, y) = (p, q, 1)^T$. It is assumed that the shading at a point on the surface depends only on its surface normal, that is, there are no cast shadows or interreflections. Under this assumption, the intensity at a point (x, y) can be modeled as $I(x, y) = R(p, q)$ where (p, q) is the gradient at (x, y).

From a calibration target with known surface geometry, the reflectance function $R(p, q)$ maps values from a two-dimensional space into a one dimensional space of intensities. In general, there are many sets of p and q that map to the same intensity value, and thus the reflectance function is not trivially invertible. To reduce ambiguities, a photometric stereo approach is used: multiple images under different illumination conditions. With three images, the problem is theoretically overconstrained, three measurements per pixel are used to estimate two gradient values:

$$\vec{I}(x, y) = \vec{R}((p(x, y), q(x, y)) \tag{2.2}$$

The reflectance functions are, in general, nonlinear functions of the gradients p and q and the inverse function is what needed, a function that maps observed intensity triples to gradients. For this, a lookup table is built.

2.4.2 Lookup Table

A lookup table is used to learn the correspondence between intensity triples and gradients. The algorithm is closest to that presented by Woodham [171], but the data is extrapolated in the table using a low-order approximation of the reflectance function, refine the gradient estimates within each bin, and handle collisions, i.e., multiple gradient pairs that produce the same intensity triple. The lookup table is three-dimensional and each bin contains a gradient and a first-order approximation of the reflectance functions in the neighborhood near the gradient.

When measuring the surface geometry of some other objects, the light intensity of different channels is known from the images. Referring to the lookup Table, the surface norm for each pixel could be gained. By solving the Poisson equation, the depth information of the each point could be obtained.

Chapter 3

Tactile Sensing using GelSight Sensors

Material perception is a big issue for robotic tactile sensors. Currently, a lot of the tactile sensors are constrained by the force feedback. There are multiple technologies for measuring the force and get the force distributions as discussed in Chapter 1. However, when interacting with the environment, material properties will matter a lot in various occasions. For example, when the robot is doing the manipulating task, it could behave more safely if it could tell the difference between soft/squishy object and hard/rigid object. For humans, it almost takes no effort to tell the differences between materials of their mechanical properties, such as softness and roughness. In this chapter, industrial methods for hardness/softness detection and roughness/smoothness detection are introduced. The possibility of using GelSight sensor to detect hardness is discussed. Also, the experiment of roughness detection using GelSight sensor is explained. Some results are shown in this chapter.

3.1 Hardness/Softness Detection

3.1.1 Industrial Methods for Hardness/Softness Detection

In industry, detecting the softness/hardness of materials is a broad area. There are a lot of commercial hardness testing machines out there to do the industrial testing, such as [74]. Also there are varieties of hardness testing scale for testing different type of materials.

1. Brinell hardness test. The Brinell scale characterizes the indentation hardness of materials through the scale of penetration of an indenter, loaded on a material testpiece. [4]

2. Vickers hardness test. The Vickers test can be used for all metals and has one of the widest scales among hardness tests. The unit of hardness given by the test is known as the Vickers Pyramid Number (HV) or Diamond Pyramid Hardness (DPH). [154]

3. Rockwell hardness test. The Rockwell test determines the hardness by measuring the depth of penetration of an indenter under a large load compared to the penetration made by a preload. [161]

4. Leeb rebound hardness test. This is a portable method, mainly used for testing sufficiently large workpieces (mainly above 1 kg). [5]

5. Knoop hardness test. The Knoop hardness test is a microhardness test - a test for mechanical hardness used particularly for very brittle materials or thin sheets, where only a small indentation may be made for testing purposes. [100]

6. Shore durometer. The durometer scale was defined by Albert F. Shore, who developed a measurement device called a durometer in the 1920s. The term durometer is often used to refer to the measurement, as well as the instrument itself. Durometer is typically used as a measure of hardness in polymers, elastomers, and rubbers. [138]

Currently two hardness tests that predominate in the rubber industry: Shore durometer and International Rubber Hardness Degrees (IRHD). The International Rubber Hardness Degrees (IRHD) test method provides a very repeatable result on rubber parts of various shapes and sizes. It is especially important in determining the hardness of rubber rings. The IRHD method employs a preliminary test load that is applied to the specimen via an indenter. The test is zeroed at this indentation position, then the total test force is applied. The distance between the two applied forces is measured and converted to an IRHD hardness value. Preliminary test forces are 8.46 gf for micro scales and 295.7 gf for regular scales. Total test forces are 15.7 gf for micro and 597 gf for regular scales [1]. The durometer hardness method is widely used in the plastic and rubber industries. The durometer method applies a predetermined test force to a spherical or conical indenter. The indenter is applied to the specimen at the test force for a predefined time period. The resulting indentation is converted into a hardness value by means of a dial gauge. Test loads range from 822 gf (A scale) to 4550 gf (D scale). Non-standard micro scales are also available. These micro scales permit testing on thin or very narrow specimens [?].

Durometer is one of several measures of the hardness of a material. The Shore hardness is measured with an apparatus known as a Durometer and consequently is also known as 'Durometer hardness'. The hardness value is determined by the penetration of the Durometer indenter foot into the sample [21]. Because of the resilience of rubbers and plastics, the hardness reading might change over time, so the indentation time is sometimes reported along with the hardness number. The ASTM test number is ASTM D2240 [?] while the analogous ISO test method is ISO 868 [3]. Durometer is typically used as a measure of hardness in polymers, elastomers, and rubbers [138].

The Durometer is the International Standard Instrument used to measure the hardness of rubber or rubber-like materials. Shore Instruments offers a wide range of durometer scales conforming to the ASTM D 2240 standard [2]. There are several scales of durometer, used for materials with different properties, among which type A and type D scales are the two most common scales. The A scale is for softer plastics,

while the D scale is for harder ones. For different scales, the testing method will be slightly different [106]. Table 3.1 shows the setting of the indenting food and applied force for Durometer Type A and Type D.

Table 3.1: Test setup for type A and D [106]

Durometer	Indenting foot	Applied mass	Resulting force
Type A	Hardened steel rod 1.1 mm - 1.4 mm diameter, with a truncated 35 cone, 0.79 mm diameter	0.822kg	8.064N
Type D	Hardened steel rod 1.1 mm - 1.4 mm diameter, with a 30 conical point, 0.1 mm radius tip	4.550kg	44.64N

In total, there are 12 scales for ASTM D 2240 [?] testing standard: A, B, C, D, DO, E, M, O, OO, OOO, OOO-S, and R. Each scale results in a value between 0 and 100, with higher values indicating a harder material [21]. For each durometer scale, specific spring forces and indentor configurations are predefined in ASTM D 2240 [?]. Table 3.2 shows the details of setup for each of these types, with the exception of Type R. [6]

Table 3.2: Durometer Scales and Testing Methods [6]

Durometer Type	Configuration	Diameter	Extension	Spring force
A	35 truncated cone	1.40 mm	2.54 mm	822 gf
C	35 truncated cone	1.40 mm	2.54 mm	4,536 gf
D	30 cone	1.40 mm	2.54 mm	4,536 gf
B	30 cone	1.40 mm	2.54 mm	822 gf
M	30 cone	0.79 mm	1.25 mm	78 gf
E	2.5 mm spherical radius	4.50 mm	2.54 mm	822 gf
O	1.20 mm spherical radius	2.40 mm	2.54 mm	822 gf
OO	1.20 mm spherical radius	2.40 mm	2.54 mm	113 gf
DO	1.20 mm spherical radius	2.40 mm	2.54 mm	4,536 gf
OOO	0.635 mm spherical radius	10.7 mm - 11.6 mm	2.54 mm	113 gf
OOO-S	10.7 mm radius disk	12.0 mm	5.0 mm	197 gf

3.1.2 Robotic Sensors for Hardness/Softness Detection

Hasegawa introduced a micromachined tactile sensor that detects both the contact force and hardness of an object. It consists of a diaphragm with a mesa structure, a piezoresistive strain sensor on the diaphragm, and a chamber for pneumatic actuation in [66]. The sensor element measures 6.0 mm 6.0 mm 0.4 mm. The fabricated tactile

sensor detected differences in hardness in the range of 10^3 to 10^5 N/m. Figure 3-1 shows the structure of our tactile sensor. It consists of a diaphragm with a mesa at the center, a piezoresistive displacement sensor at the periphery, and a chamber for pneumatic actuation. Figure 3-2 shows an array of three sensor elements.

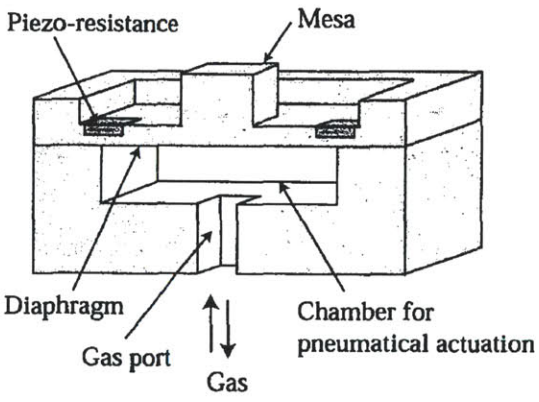

Figure 3-1: Structure of the tactile sensor [66]

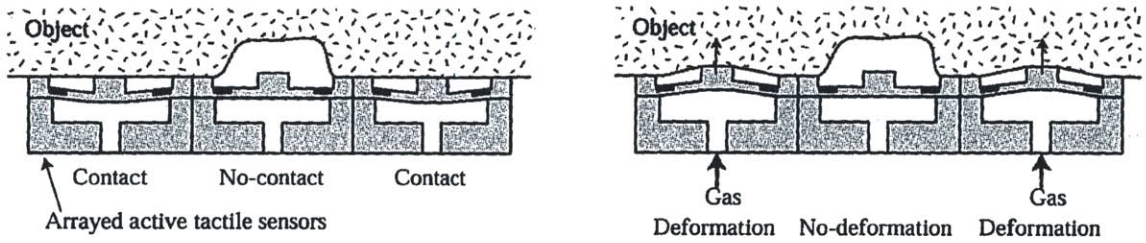

Figure 3-2: (a) Detecting contact force distribution and two dimentional surface image. (b) Detecting hardness distribution. [66]

When the tactile sensor array makes contact with an object having a bumpy surface (Figure 3-2a), the surface profile of the object causes some of the mesa structures on the diaphragms to contact the object, so their diaphragms deform downwards. From the displacement and location of the deformed diaphragms, the system can detect the contact-force distribution and 2D surface texture image of the object. Hardness distribution detection In the second mode, the contacted mesa elements are pneumatically driven against the object (Figure 3-2b). The contacted regions of

the object are deformed according to the driving force of the mesa element and the hardness of the object (Figure 3-3). Therefore, we can detect the hardness distribution of the object by measuring the relationship between the displacements of the diaphragms and the actuation force of the mesa elements.

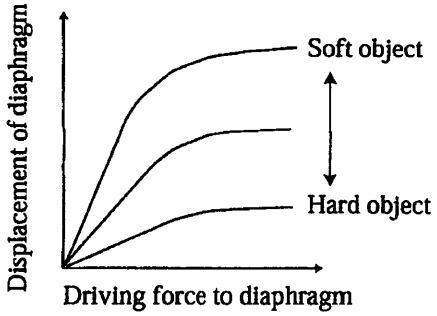

Figure 3-3: Displacement of a diaphragm as a function of the hardness of the object [66]

3.2 Roughness/Smoothness Detection

Surface roughness, often shortened to roughness, is a measure of the texture of a surface. It is quantified by the vertical deviations of a real surface from its ideal form. If these deviations are large, the surface is rough; if they are small the surface is smooth. Roughness is typically considered to be the high frequency, short wavelength component of a measured surface.

Roughness plays an important role in determining how a real object will interact with its environment. Rough surfaces usually wear more quickly and have higher friction coefficients than smooth surfaces. Roughness is often a good predictor of the performance of a mechanical component, since irregularities in the surface may form nucleation sites for cracks or corrosion.

Although roughness is usually undesirable, it is difficult and expensive to control in manufacturing. Decreasing the roughness of a surface will usually increase exponentially its manufacturing costs. This often results in a trade-off between the manufacturing cost of a component and its performance in application.

A roughness value can either be calculated on a profile or on a surface. The profile roughness parameter (R_a, R_q) are more common. The area roughness parameters (S_a, S_q) give more significant values. Each of the roughness parameters is calculated using a formula for describing the surface. There are many different roughness parameters in use, but it is by far the most common. Some parameters are used only in certain industries or within certain countries. For example, the family of parameters is used mainly for cylinder bore linings, and the Motif parameters are used primarily within France. Since these parameters reduce all of the information in a profile to a single number, great care must be taken in applying and interpreting them. Small changes in how the raw profile data is filtered, how the mean line is calculated, and the physics of the measurement can greatly affect the calculated parameter.

By convention every 2D roughness parameter is a capital R followed by additional characters in the subscript. The subscript identifies the formula that was used, and the R means that the formula was applied to a 2D roughness profile. Different capital letters imply that the formula was applied to a different profile. For example, R_a is the arithmetic average of the roughness profile, P_a is the arithmetic average of the unfiltered raw profile, and S_a is the arithmetic average of the 3D roughness. Each of the formulas assumes that the roughness profile has been filtered from the raw profile data and the mean line has been calculated. The roughness profile contains n ordered, equally spaced points along the trace, and y_i is the vertical distance from the mean line to the i^{th} data point. Height is assumed to be positive in the up direction, away from the bulk material. [47]

The definition of common used roughness parameter is shown below: [14]

Arithmetical mean roughness (R_a): A section of standard length is sampled from the mean line on the roughness chart. The mean line is laid on a Cartesian coordinate system wherein the mean line runs in the direction of the x-axis and magnification is the y-axis. The value obtained with the formula below is expressed in micrometer (um).

$$R_a = \frac{1}{n}\sum_{i=1}^{n}|y_i| \tag{3.1}$$

Maximum peak (R_y): A section of standard length is sampled from the mean line on the roughness chart. The distance between the peaks and valleys of the sampled line is measured in the y direction. The value is expressed in micrometer.

$$R_q = \sqrt{\frac{1}{n}\sum_{i=1}^{n}y_i^2} \tag{3.2}$$

Ten-point mean roughness (R_z): A section of standard length is sampled from the mean line on the roughness chart. The distance between the peaks and valleys of the sampled line is measured in y direction. Then, the average peak is obtained among 5 tallest peaks(Y_p), as the average valley between 5 lowest valleys (Y_v). The sum of these two values is expiressed in micrometer.

$$R_z = \frac{|Y_{p1}+Y_{p2}+Y_{p3}+Y_{p4}+Y_{p5}|+|Y_{v1}+Y_{v2}+Y_{v3}+Y_{v4}+Y_{v5}|}{5} \tag{3.3}$$

3.2.1 Industrial Methods for Roughness/Smoothness Detection

Human perception is highly relative. In other words, without something to compare to, you will not be certain about what you are feeling. To give the human tester a reference for what they are touching, commercial sets of standards are available. Comparison should be made against matched identical processes. One method of note is the finger nail assessment of roughness and touch method used for draw dies in the auto industry.

In industry, roughness of a certain material is measured using a mechanical stylus. One example of this is the Brown and Sharpe Surfcom unit. Basically this technique uses a stylus that tracks small changes in surface height, and a skid that follows large changes in surface height. The use of the two together reduces the effects of non-flat

surfaces on the surface roughness measurement. The relative motion between the skid and the stylus is measured with a magnetic circuit and induction coils.

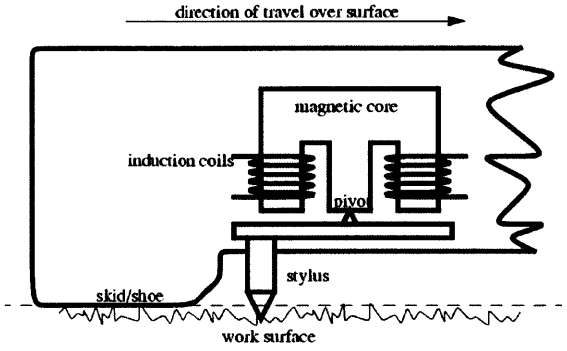

Figure 3-4: Industrial Roughness measurement principle [162]

The actual apparatus uses the apparatus hooked to other instrumentation. The induction coils drive amplifiers, and other signal conditioning hardware. The then amplified signal is used to drive a recorder that shows stylus position, and a digital readout that displays the CLA/Ra value.

The datum that the stylus position should be compared to can be one of three

- Skid - can be used for regular frequency roughness
- Shoe - can be used for irregular frequency roughness
- Independent - can use an optical flat

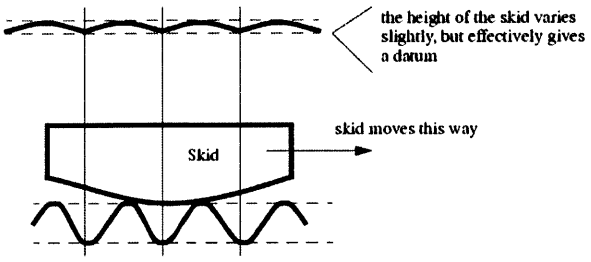

Figure 3-5: Skid - used for regular frequencies, and very common. [162]

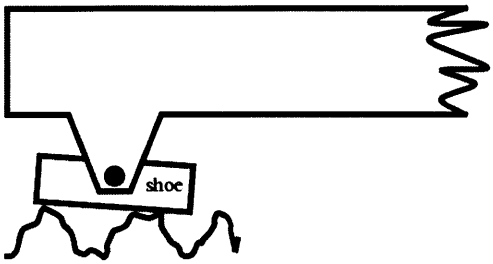

Figure 3-6: Flat Shoe - used for surfaces with irregular frequencies. [162]

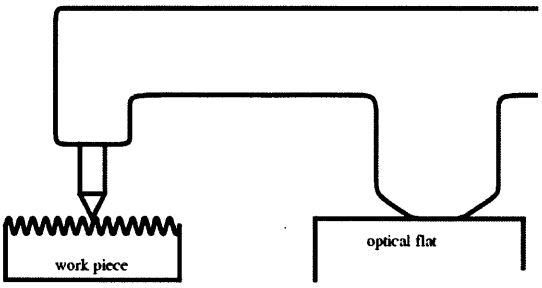

Figure 3-7: Independent Datum - used for surface texture varies within a very small section of the surface.[162]

3.2.2 Robotic Sensors for Roughness/Smoothness Detection

Traditionally, an accelerometer and a mechanical probe are used to detect roughness of a surface [173]. While the mechanical probe goes along the detected surface, the accelerometer connected to the probe is used to measure the frequency of vibration the probe generated while sliding across the surface. From the frequency and vibration magnitude, the roughness of the surface could be inferred. [96]

3.3 Tactile Perception using Elastomeric Sensor

3.3.1 My work in Hardness/Softness Detection

3.3.1.1 Samples used in Hardness/Softness Detection

Samples used for the hardness detection experiment are rubbers with different ShoreA scale softness and Shore00 scale softness. ShoreA scale is used for relative hard materials and Shore00 scale is used for relative soft materials.

For ShoreA 30, ShoreA 40 and ShoreA 50 (the larger number, the harder the material) samples, I cast them into the same shape using the materials bought from Smooth-On Inc [156]. The shape is shown in the figuer 3-8a. Also, two relative soft samples, made of the material bought from Smooth-On Inc [155] are with softness Shore00-10 and Shore00-30 (the larger number, the harder the material) respectively. The shape of Shore00 samples is cylinders with 35 mm in diameter and 20 mm in depth as shown in 3-8b.

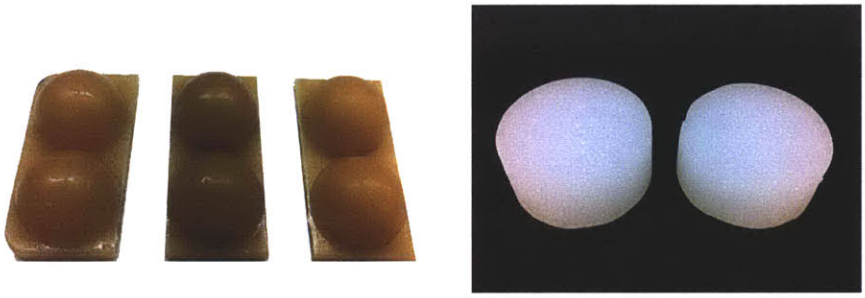

(a) (b)

Figure 3-8: Samples for hardness detection experiment. (a) shows the samples of ShoreA scale, from left to right, ShoreA 30, ShoreA 40, ShoreA 50. (b) shows the samples of Shore00 scale, from left to right, Shore00 10, Shore00 30

3.3.1.2 Result for Hardness/Softness Detection

For materials with different softness, the simplest way to measure the softness is to find the relationship of force and displacement while doing the indentation task. Here I prepare three rubber objects of same shape but different softness. Using Durameter scale, the softness of the samples is ShoreA 30, ShoreA 40 and ShoreA 50, respectively. Using the 2000N load Instron indentation machine, 10,000 data points are recorded within 10mm indentation. Here I plot the relationship of force applied to each object and the displacement occurred to the object. From the figure, we could tell, by combining the force feedback and displacement feedback, it's possible to detect the softness of a material.

As shown in Figure 3-10, two cylinder samples with same shape but different softness are measured using the same technique. The softness of the two samples are

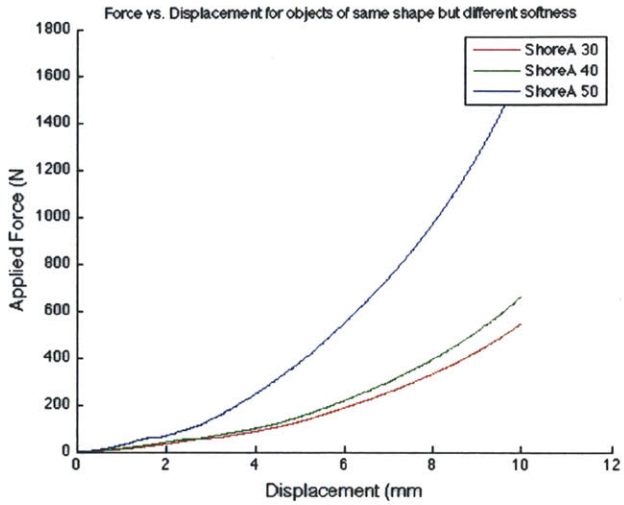

Figure 3-9: Force vs. Displacement of the objects with same shape but different softness

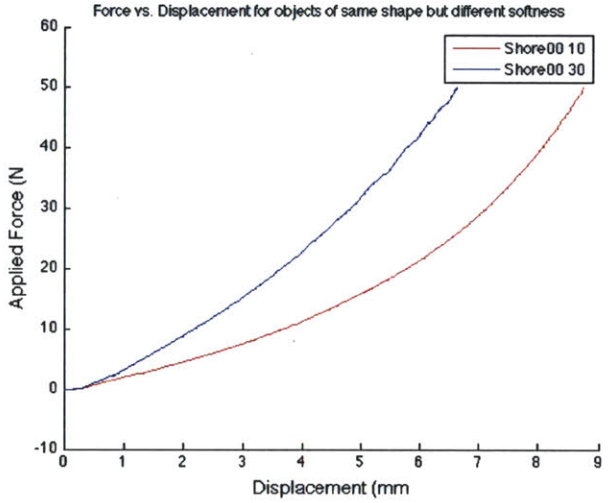

Figure 3-10: Force vs. Displacement of the objects with same shape but different softness

Shore00-10, Shore00-30, respectively.

By measuring the stress and strain relationship of our GelSight sensor, we could know the mechanical property of the sensor itself. Since from our technique, we could reconstruct the depth information occurred in the sensor, so the displacement could be obtained. With the displacement and sensor's mechanical properties, using Finite Element Analysis, the force applied on the sensor could be calculated. However, the mechanical property of the sensor will change over time and usage. In the Figure

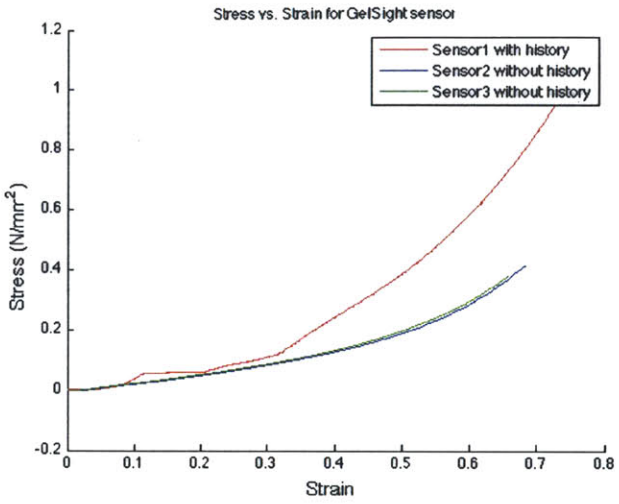

Figure 3-11: Strain vs. Stress of GelSight sensors

3-11, the blue and green line shows the stress over strain for the fresh sensors, but for the sensor that has a lot of history, the red curve shows that the mechanical property differs a lot. In principle, it is possible for GelSight sensor to extract the force distribution information of the contacting surfaces, but the history of the sensor should be taken into consideration while extracting force distribution from the depth information. Due to time limitation, there is no further analysis done for this thesis.

3.3.2 My work in Roughness/Smoothness Detection

GelSight sensor could obtain the surface geometry, which makes the roughness detection task feasible. As described in Session 3.2, Equation 3.3 is the deviation the sampled depths data in one direction.

3.3.2.1 Samples used in Roughness/Smoothness Detection

In the Roughness/Smoothness Detection experiment, sandpapers of different grit are used. 50 grit, P80 grit, 150 grit, 320 grit and P500 grit are the five samples used in this task, as shown in the Figure 3-12. From [97], we could know that for roughness value, 50 grit > P80 grit > 150 grit > 320 grit > P500 grit. All the sandpaper samples here are purchased from McMaster-Carr [121].

Figure 3-12: Samples for roughness detection experiment. Here shows the samples of sandpaper used in the experiment, from left to right, 50 grit, P80 grit, 150 grit, 320 grit and P500 grit

3.3.2.2 Roughness/Smoothness Detection Experiment

Sensor used for roughness detection is GelSight Portable device, as shown in Figure 2-7c. There are five types of sandpapers, six patches for each type. In total, there are 30 samples. For each sample, the surface geometry is obtained using the portable device. For each surface geometry, R_a for each row and each column is calculated using the Equation 3.3. Then all the R_a value is averaged to get the representative R_a for each patch.

Table 3.3: Roughness Estimation Result for Sandpaper Samples R_a

Sample(grit)	Patch1	Patch2	Patch3	Patch4	Patch5	Patch6
50	1.1293	1.1771	1.1293	1.1530	1.1132	1.1247
P80	0.8124	0.8209	0.7767	0.8203	0.7875	0.7688
150	0.5390	0.5446	0.5606	0.5747	0.5575	0.5513
320	0.4345	0.4375	0.3878	0.4508	0.4321	0.4168
P500	0.3648	0.3699	0.3786	0.3650	0.3796	0.3664

As shown in Table 3.3, each row is the R_a value for the same type of sandpaper, but different patches. From the data, we could see that for the same type of sandpaper, the R_a value tend to cluster together. To make it more visible, I fit a plot the bar chart for five data points gained from each type of the sandpaper samples, and error bar is also shown in Figure 3-13

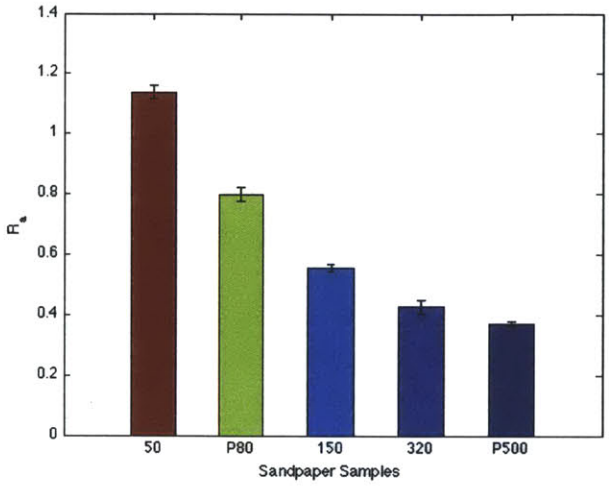

Figure 3-13: R_a distribution of the sandpaper samples tested in the experiment, from left to right, 50 grit, P80 grit, 150 grit, 320 grit and P500 grit

3.3.2.3 Conclusion for Roughness/Smoothness Detection Experiment

GelSight sensor is able to compare the roughness of the selected sandpaper successfully. From the R_a distribution of different sandpaper samples, there is almost no overlap for each distribution curve, which means they could be distinguished with a very high accurate probability. There are still several issues that need to be figured out. First is how to match R_a value gained from GelSight sensor with physical R_a in the industrial world. Second is whether the roughness comparison method will work with other materials. More sandpaper could be tested using the same method. Also it will be very interesting to compare the roughness of soft materials, such as rubber, foam and etc.

Chapter 4

Tactile Sensor Application – Detection of Lumps in Soft Tissue

Using the distributed tactile receptors embedded in the skin, humans can localize lumps in soft tissue. By the processing between fingers and brain, human can give feedback of the presence or absence of the lump. However, this type of task becomes challenging when human body has no direct contact with the tissue, such as in laparoscopic or robot-assisted procedures. [65]

Tactile sensors have been proposed to characterize and detect lumps in robot-assisted palpation. However, there is no tactile sensor that could provide enough tactile information to the user. Using GelSight sensor as described in the previous chapter, a lump detection experiment is conducted. In this experiment, a visual display of tactile information is presented. Also, a simple threshold method is introduced for binary feedback of lump detection. Similar task is performed by human subjects. The performance of GelSight sensor and human subjects in lump detection is compared. Furthermore, the effects of various tissue parameters (lump size, lump depth, and surrounding tissue stiffness) is discussed on the performance of both the human finger and the tactile sensor. Last, the performance of Gelsight sensor is compared with DigiTacts sensor [65].

4.1 Introduction

Tactile sensation is very important for medical examination. Surgeons depend on tactile sensation to guide manipulation and exploration in open surgery [111]. Lumps, for example, is typically the case, as hard tissue (lump) in the soft tissues of the breast, prostate, lungs, and other tissues [44]. [73], [104], [136] have shown that lumps are significantly stiffer than surrounding tissue. This contrast of stiffness helps a lot in the localization and assessment of lumps during open surgery, when the surgeons fingertips are in direct contact with the tissue and tactile information is readily available [65]. As minimally invasive surgery (MIS) or robot-assisted minimally invasive surgery (RMIS) being used more often, the direct tactile sensation to guide the surgeon is deprived. Even though these techniques have increased dexterity, precision and control, they eliminate the surgeons natural tactile feedback, which makes palpation for lumps more difficult, especially because these structures are often beneath the tissue surface and cannot be detected visually [65].

Detection of lumps using tactile sensors is still a challenging problem. Peine and Howe [133] evaluated the abilities of humans to detect hard lumps in soft tissue, with varying lump sizes and indentation velocities. They found that subjects sensed the deformation of the finger pad induced by the lump itself, and not the changes in finger pad pressure distribution. In [65], a study of robotic sensor lump detection comparing to human lump detection is conducted. They found that their sensor outperform human when human behaves as a passive explorer. In this chapter, I will talk about my experiment in lump detection using GelSight sensor and human psychological experiment while doing similar task. The performance of GelSight sensor and human is evaluated when human behaves as an active explorer.

4.2 Lump Detection Using GelSight Sensor

4.2.1 Experiment Phantoms

Phantoms were created to simulate hard lumps in soft tissue. Models were molded from Ecoflex 00-10 (softer) and 00- 30 (harder) silicone rubber (Smooth-on Inc, Easton PA), where the suffix number represents the rubber hardness on the Shore 00 scale [21]. Models were shaped as cylinder blocks measuring approximately 35 mm in diameter and 20 mm in height. Lumps were made of Delrin as spheres with diameters of 2mm, 3mm, 5mm, 8mm and 9.5 mm, and were embedded below the surface of the tissue at depths of 1, 2, 3, 4, 5 and 6 mm. All the dimensions are shown in Figure 4-1. The combination of two rubber hardness (Shore 00-10, 00-30), six lump depths, and five lump sizes produce 60 distinct phantom models. A table of both model sets is shown in Figure 4-2. 60 additional models without a lump is made, served as baseline models, 30 for each hardness. Delrin is harder than most cancerous tissue, but provides a good contrast against the soft rubber for the purposes of this study. While tissue is difficult to model accurately due to its heterogeneity and variance according to location, we chose materials to represent tissue (ecoflex silicone rubber) and lumps (Delrin) which reasonably approximate an average equivalent contrast in stiffness to that found for lumps in breast [105] and prostate [76], [176] tissues. The materials used for phantoms in this experiment are the same as the materials used in [65].

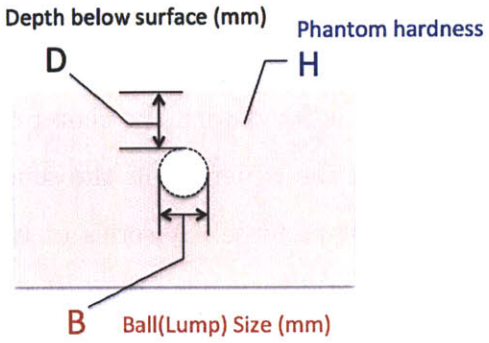

Figure 4-1: Physical description of phantom samples.

(mm)	00-10 (H10)					00-30 (H30)				
	B1	B2	B3	B4	B5	B1	B2	B3	B4	B5
	2	3	5	8	9.5	2	3	5	8	9.5
D1	1	1	1	1	1	1	1	1	1	1
D2	2	2	2	2	2	2	2	2	2	2
D3	3	3	3	3	3	3	3	3	3	3
D4	4	4	4	4	4	4	4	4	4	4
D5	5	5	5	5	5	5	5	5	5	5
D6	6	6	6	6	6	6	6	6	6	6

Figure 4-2: Samples differ in lump size (ball, B), embedded lump depth (depth, D), and hardness of surrounding materials (hardness, H). All 60 models are represented in the table with dimensions in mm. The notation shown here is used throughout this chapter

4.2.2 Experiment Setup

GelSight portable device, as shown in Figure 2-7c, is used for lump detection experiment. As talked about in Chapter1, the sensor is using a 0.8 megapixel Point Grey Flea2 firewire camera (1032 $\times$ 776 pixels). The configuration of the camera used in this experiment is 640 $\times$ 480 pixels, 15 frames per second, 6.00 shutter speed.

The setup of the experiment is shown in the Figure 4-3. The phantom is placed in the middle of the scale, which is fixed by the blue part in the photo. Above the sample, GelSight portable device is fixed with the center of the sensor lined up with the center of the sample. During the experiment, the sensor will be pressed against the sample with different amount of force. A series of images will be taken under the directional illumination of portable device. From the series of images, using the lookup table built from a calibration target with know surface geometry, the depth information occurred on the sensor will be reconstructed (For details, please refer to Chapter2).

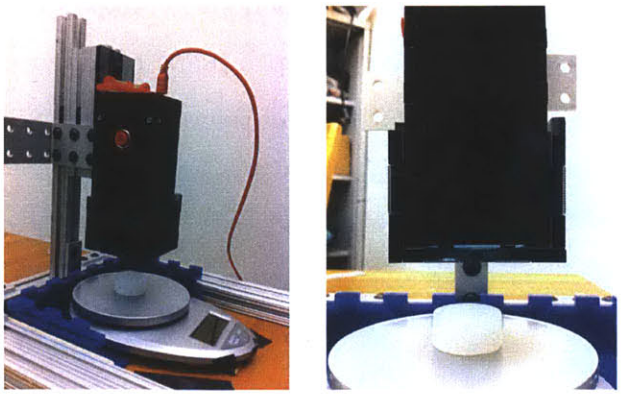

(a) (b)

Figure 4-3: Here shows the Setup for the robotic experiment.

4.2.3 Robotic Experiment Methodology

In the experiment, I'm experimenting with phantom samples with different softness, different sizes of the lump, different depth the lump embedded in the tissue and different forces applied on the sample. For each trial, the depth information is reconstructed from GelSight sensor (For reconstruction algorithm, please refer to Chapter 2).

Since we have many samples, to make the illustration clear, I numerate the sample with the information of softness, depth, lump size. For example, H30-D4-B9.5 indicates the sample consists of Shore00 30 tissue and a lump sized 9.5 mm embedded at 4mm away from the surface. Sometimes, force information will be added to the sample, such as H30-D4-B9.5-F2500 means H30-D4-B9.5 sample is pressed using force of $2500g$. The unit used for length is mm, and unit used for force units is $gram$.

4.2.3.1 Blank Samples

As mentioned in previous session, there are 30 blank samples for each softness. From the H30 blank samples, five of them are picked as the control group. For each blank sample, five different forces are applied. The forces are 500g, 1500g, 2500g, 3500g and 4500g, respectively. In 4-4, shows the depths information for all the trials tested on the blank samples. We could see that there are some depth variation even for the

blank samples. These information might influence the lump detection result. To have the control line for each force, I average depth maps of different samples with the same force, then get the averaged depth map for forces, which is shown in Figure4-5. I will take the average depth map as a baseline for future comparison.

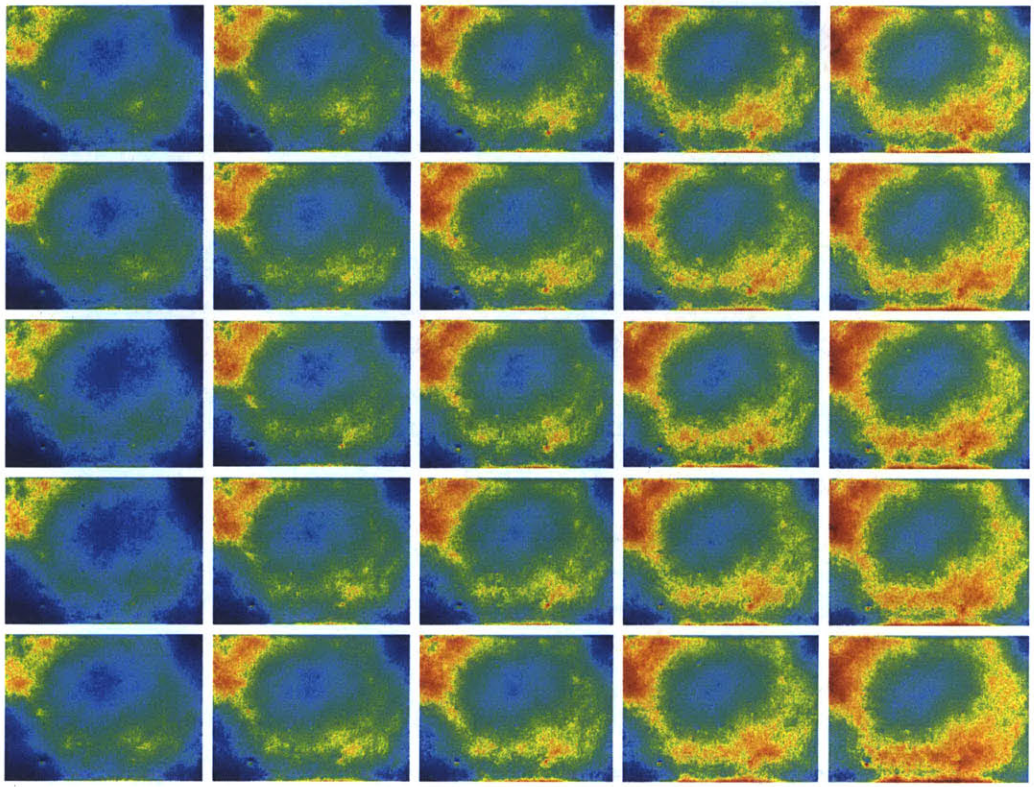

Figure 4-4: Depth map for different blank samples while pressed by different forces. Each row is the same sample with different force, while each column is the same force applied on different blank samples. From left to right, the forces applied on the sample are 500g, 1500g, 2500g, 3500g and 4500g, respectively.

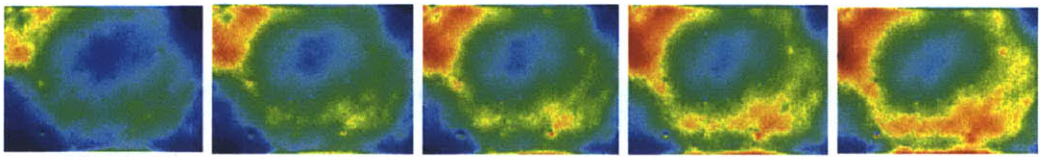

Figure 4-5: Average depth map over different blank samples at the same force. From left to right, the forces are 500g, 1500g, 2500g, 3500g and 4500g, respectively.

4.2.3.2 Samples with different applied forces

From Figure 4-5, we could tell that forces applied on the sample will influence the result of depth map. Here I pick phantom samples with medium lump size (5mm) embedded at a medium depth (3mm) (H30-D3-B5) as illustration.

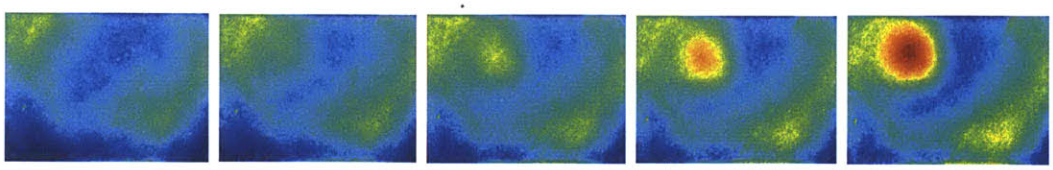

Figure 4-6: Depth map of H30-D3-B5 while pressed with different forces. From left to right, the forces are 500g, 1500g, 2500g, 3500g and 4500g, respectively.

As shown in 4-5, even for blank samples, there are some depth variation. To clean up the depth map, I subtract the sample depth map with the average blank sample depth map of the same force, as shown in Figure 4-7. Simply by looking at the depth map, we could see that there is a clear red circular region in the derivation depth map for H30-D3-B5-F2500, while in the original depth map, it's hard to tell. Also for H30-D3-B5-F1500, the signal of the lump is mixed together with the background in the original depth map, while there is a small yellow region in the derivation depth image.

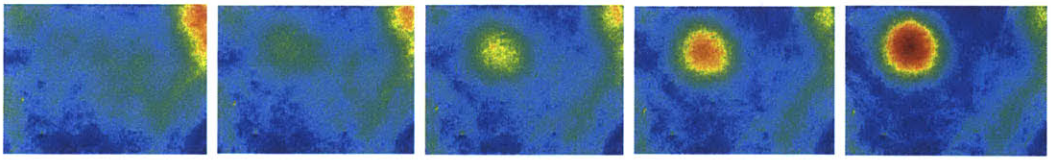

Figure 4-7: Depth map derivation of H30-D3-B5 pressed with different forces from the blank sample. From left to right, the forces are 500g, 1500g, 2500g, 3500g and 4500g, respectively.

Here shows more comparison of original depth images with the deviative depth images from the average blank sample depth image.

From all the figures shown here, the deviative depth map is easier to tell the presence of the lump. Also, the larger the force, the stronger the contract is in the depth map.

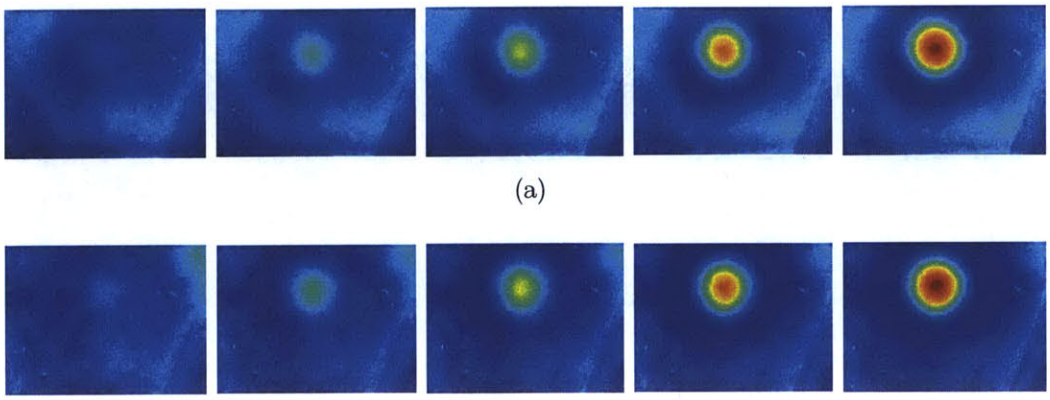

(a)

(b)

Figure 4-8: H30-D1-B5 with different force applied. (a) Original depth map (b) Derivative depth map. From left to right, the forces are 500g, 1500g, 2500g, 3500g and 4500g, respectively.

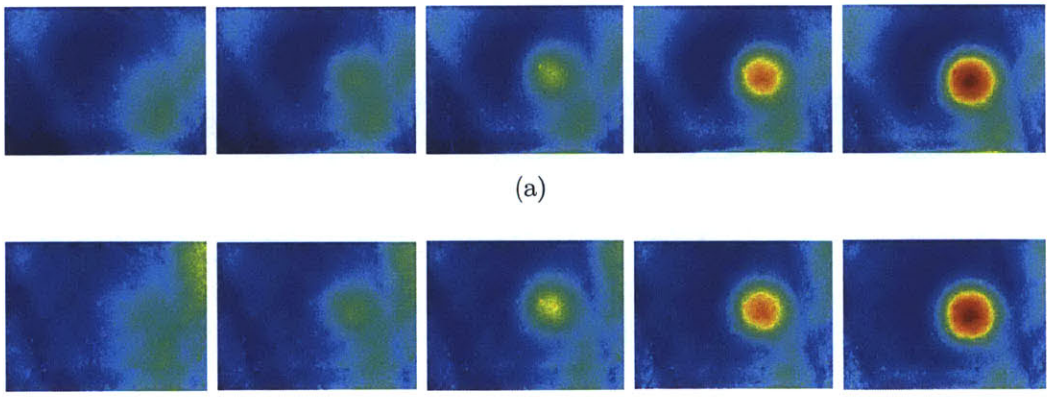

(a)

(b)

Figure 4-9: H30-D2-B5 with different force applied. (a) Original depth map (b) Derivative depth map. From left to right, the forces are 500g, 1500g, 2500g, 3500g and 4500g, respectively.

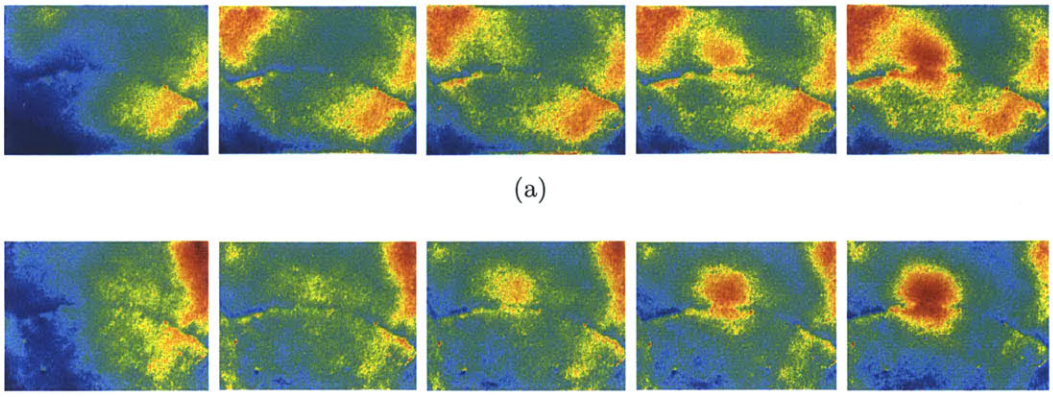

(a)

(b)

Figure 4-10: H30-D4-B5 with different force applied. (a) Original depth map (b) Derivative depth map. From left to right, the forces are 500g, 1500g, 2500g, 3500g and 4500g, respectively.

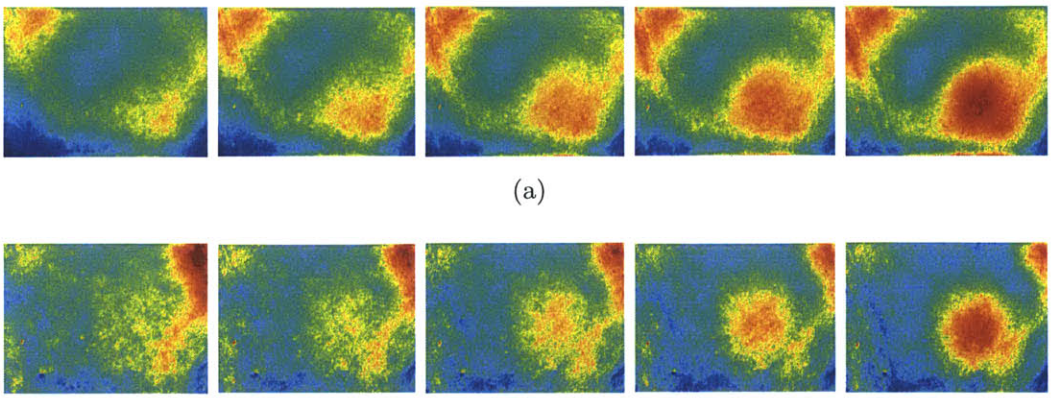

(a)

(b)

Figure 4-11: H30-D5-B5 with different force applied. (a) Original depth map (b) Derivative depth map. From left to right, the forces are 500g, 1500g, 2500g, 3500g and 4500g, respectively.

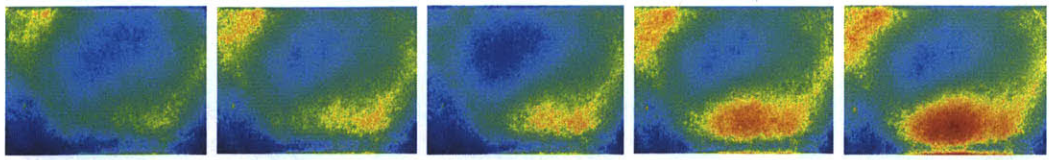

(a)

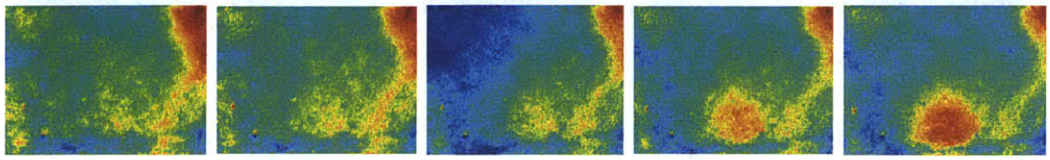

(b)

Figure 4-12: H30-D6-B5 with different force applied. (a) Original depth map (b) Derivative depth map. From left to right, the forces are 500g, 1500g, 2500g, 3500g and 4500g, respectively.

4.2.3.3 Samples with different sized lumps

To see how lumps with different sizes could influence the depth map, here I pick phantom samples with lump size embedded at a medium depth (3mm) while pressed with the same force (H30-D3-F4500) as illustration.

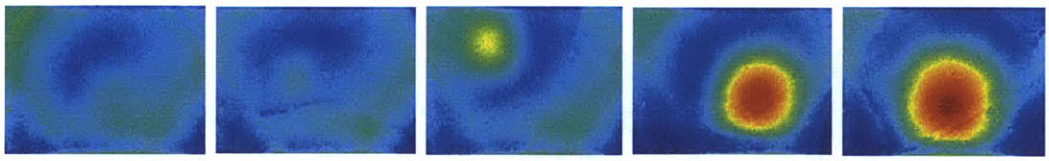

Figure 4-13: Depth map of H30-D3-F4500 with lump of different sizes. From left to right, the sizes of the lumps are 2mm, 3mm, 5mm,8mm and 9mm respectively.

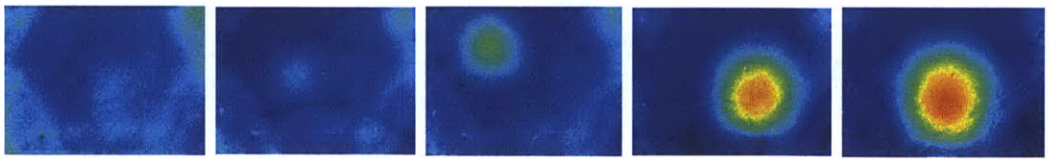

Figure 4-14: Depth map derivation of H30-D3-F4500 pressed with different sized lumps. From left to right, the sizes of the lumps are 2mm, 3mm, 5mm, 8mm and 9mm respectively.

To clean up the depth map, I subtract the depth map with the average blank

sample depth map of the same force, shown in Figure 4-15b. Simply by looking at the depth map, lumps in B5 is easy to tell in the derivative depth map while in the orginal image, it's hard to tell it apart from the background. Same case is for the B3 sample. Also, sample with larger lumps, the contrast of the lump location from the tissue is stronger.

Here shows more comparison examples for samples with lump of different sizes.

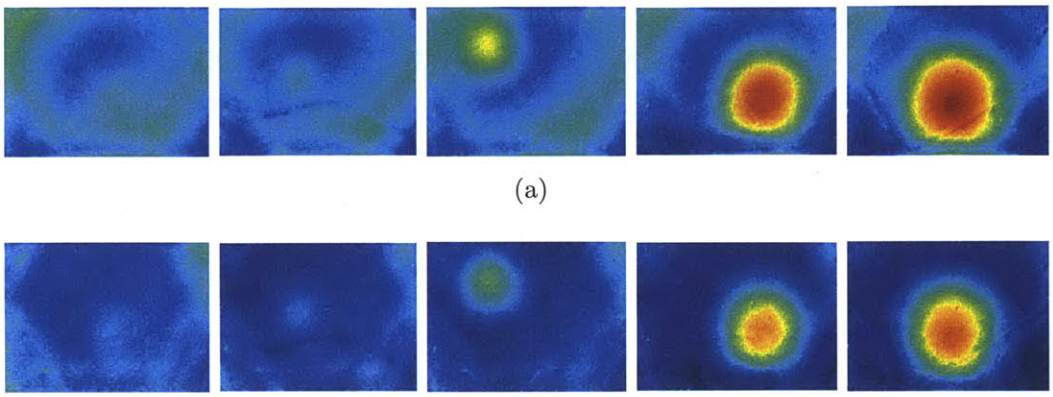

(a)

(b)

Figure 4-15: H30-D3-F4500 samples with lump of different sizes. (a) Original depth map (b) Derivative depth map. From left to right, the sizes are B2, B3, B5, B8 and B9.5, respectively.

From all the figures shown here, the deviative depth map is easier to tell the presence of the lump. Also, the bigger the lump is, the stronger the contrast is.

4.2.3.4 Samples with lumps embedded at different depths

To see how the depths of lumps could influence the depth map, here I pick phantom samples with medium sized lump (B5). All the samples are pressed with the same force (F4500).

To clean up the depth map, I subtract the depth map with the average blank sample depth map of the same force, shown in Figure 4-22. Simply by looking at the depth map, all the lumps is easy to tell in the derivative depth map while in the orginal image, it's hard to tell it apart when the depth is getting deepter. For sample

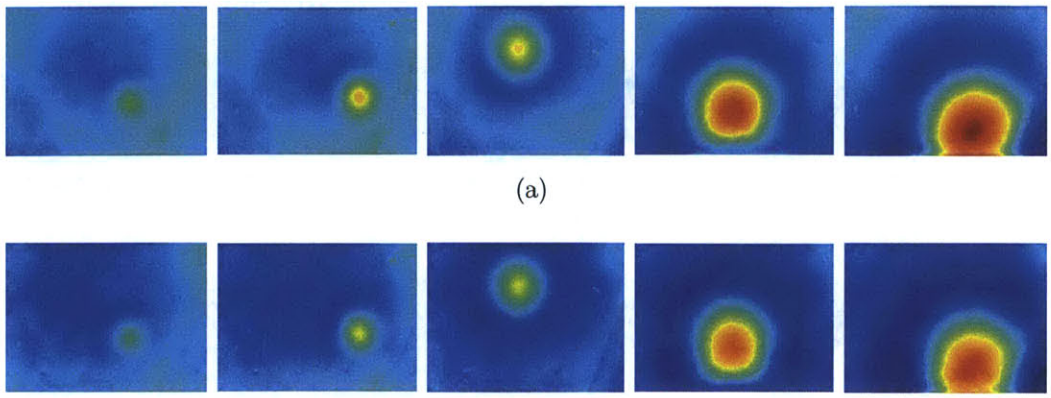

(a)

(b)

Figure 4-16: H30-D1-F4500 samples with lump of different sizes. (a) Original depth map (b) Derivative depth map. From left to right, the sizes are B2, B3, B5, B8 and B9.5, respectively.

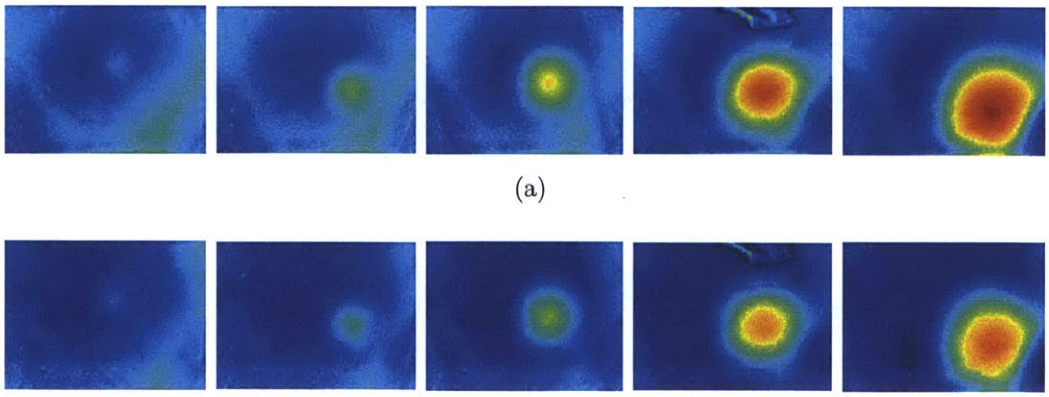

(a)

(b)

Figure 4-17: H30-D2-F4500 samples with lump of different sizes. (a) Original depth map (b) Derivative depth map. From left to right, the sizes are B2, B3, B5, B8 and B9.5, respectively.

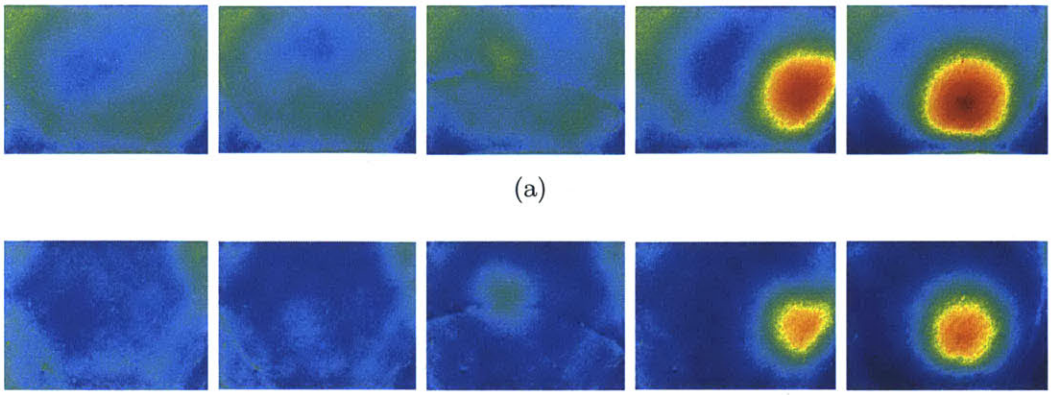

(a)

(b)

Figure 4-18: H30-D4-F4500 samples with lump of different sizes. (a) Original depth map (b) Derivative depth map. From left to right, the sizes are B2, B3, B5, B8 and B9.5, respectively.

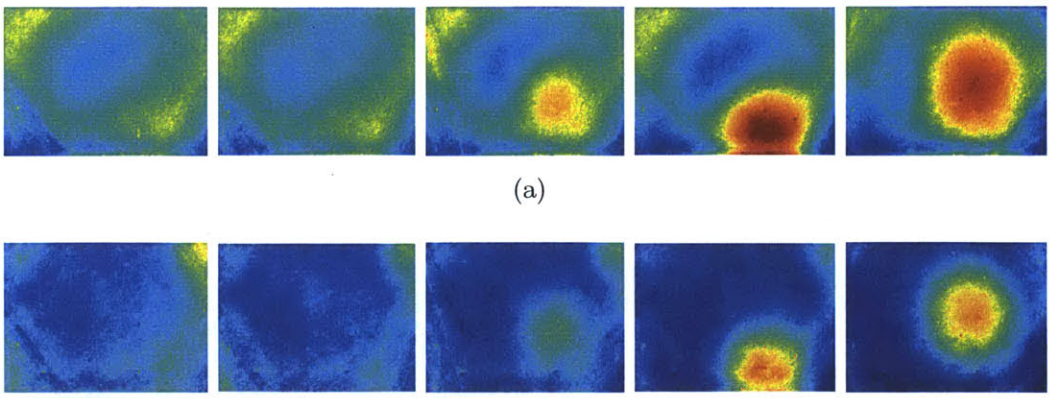

(a)

(b)

Figure 4-19: H30-D5-F4500 samples with lump of different sizes. (a) Original depth map (b) Derivative depth map. From left to right, the sizes are B2, B3, B5, B8 and B9.5, respectively.

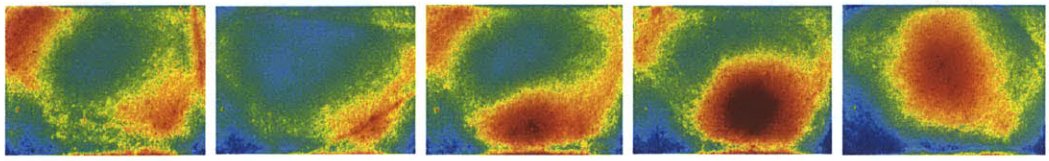

(a)

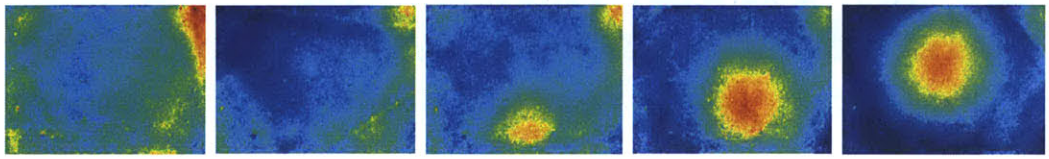

(b)

Figure 4-20: H30-D6-F4500 samples with lump of different sizes. (a) Original depth map (b) Derivative depth map. From left to right, the sizes are B2, B3, B5, B8 and B9.5, respectively.

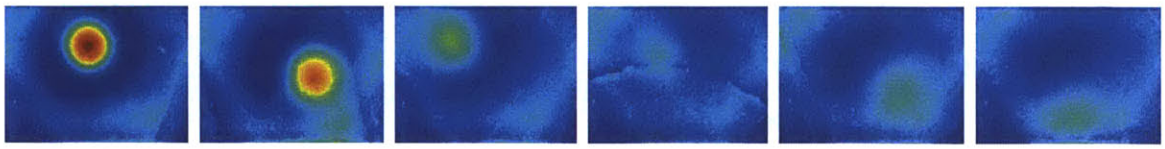

Figure 4-21: Depth map of H30-B5-F4500 with different lump embedded at different depths. From left to right, the depths are D1, D2, D3, D4, D5 and D6 respectively.

with same sized lumps, the contrast of the lump from surroundings is getting less as depth increases.

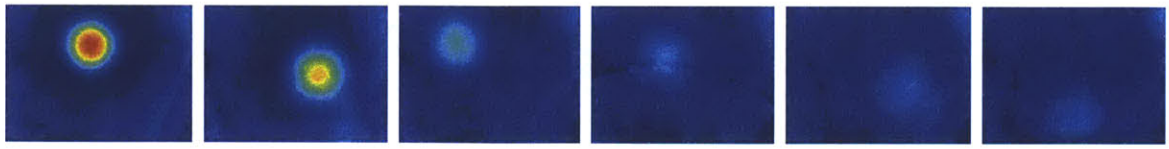

Figure 4-22: Derivative depth map of H30-B5-F4500 with different lump embedded at different depths. From left to right, the depths are D1, D2, D3, D4, D5 and D6 respectively..

Here shows more comparison examples for samples with lumps embedded at different depths.

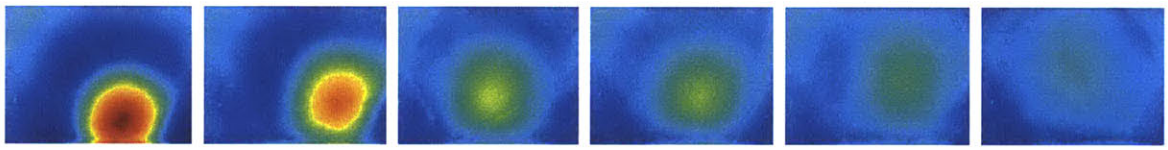

(a)

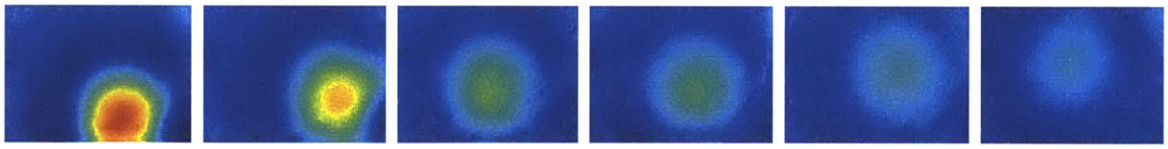

(b)

Figure 4-23: H30-B9-F4500 samples with the lump embedded at different depths. (a) Original depth map (b) Derivative depth map. From left to right, the depths are D1, D2, D3, D4, D5 and D6, respectively.

From all the figures shown above, the deviative depth map is easier to tell the presence of the lump. Also, the deeper the lump is embedded, the weaker the contrast of the lump is.

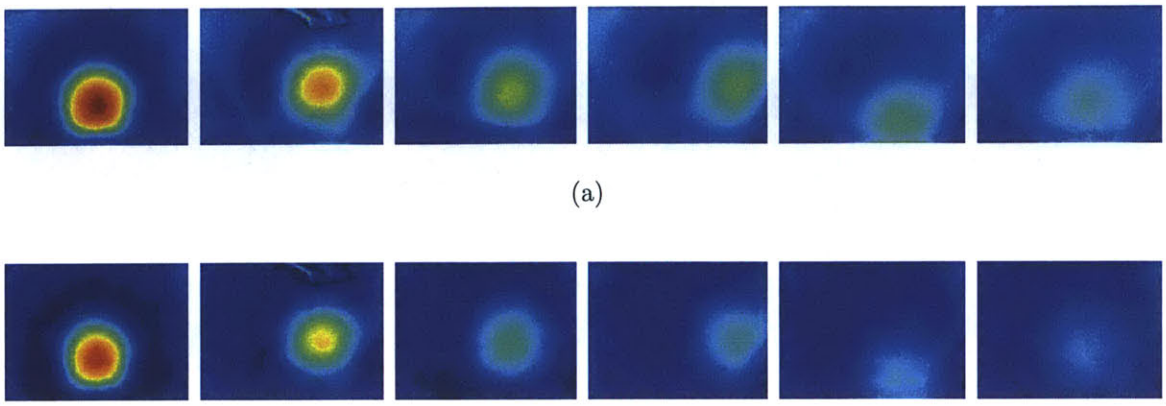

(a)

(b)

Figure 4-24: H30-B8-F4500 samples with the lump embedded at different depths. (a) Original depth map (b) Derivative depth map. From left to right, the depths are D1, D2, D3, D4, D5 and D6, respectively.

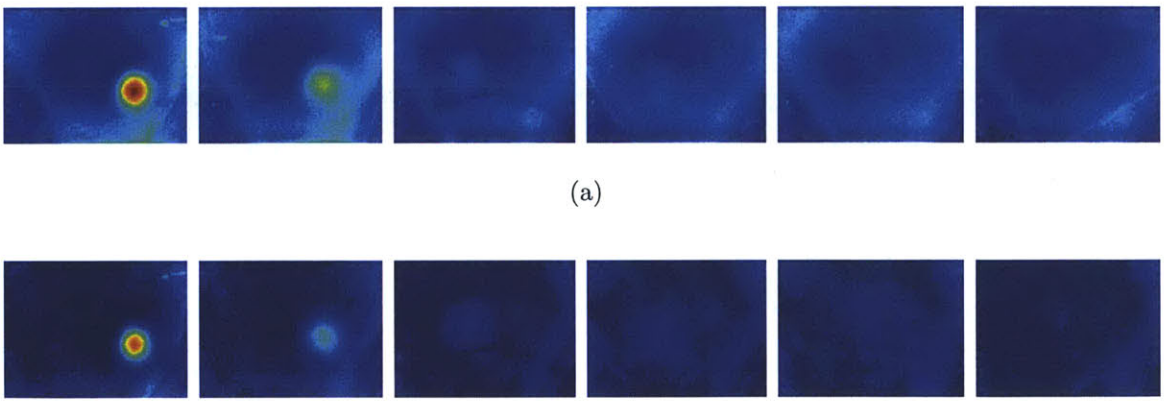

(a)

(b)

Figure 4-25: H30-B3-F4500 samples with the lump embedded at different depths. (a) Original depth map (b) Derivative depth map. From left to right, the depths are D1, D2, D3, D4, D5 and D6, respectively.

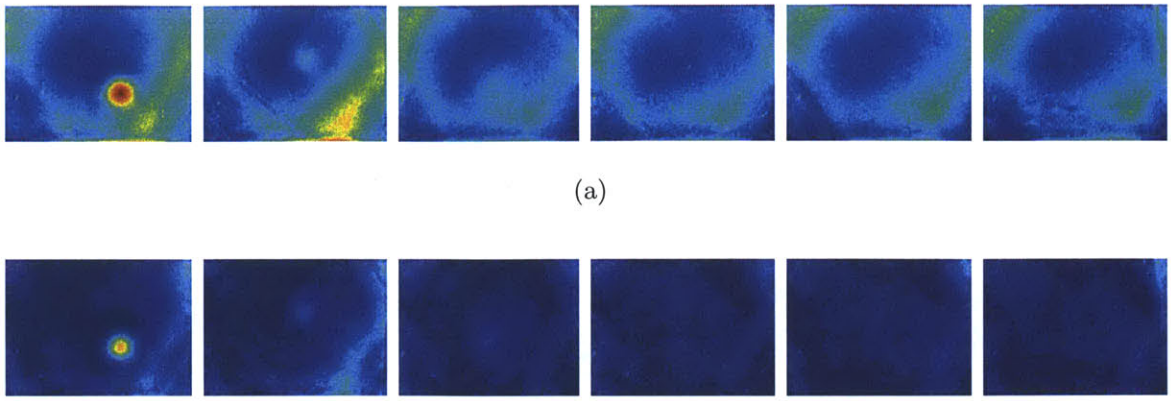

(a)

(b)

Figure 4-26: H30-B2-F4500 samples with the lump embedded at different depths. (a) Original depth map (b) Derivative depth map. From left to right, the depths are D1, D2, D3, D4, D5 and D6, respectively.

4.2.3.5 All Samples

From previous discussion, we know that the derivative depth map is more informative comparing to the original depth image. Also force is a major factor for lump detection preformance. Here I show the derivative depth map for all the H30-F4500 samples in Figure 4-27

Simply by looking at the depth images, human could have the judgement of the presence of lump. From Figure 4-27, the judgement of lump becomes challenging while the lump is getting smaller and the depth getting deeper. For B9, B8 and B5, the presence of the lump could be detected easily. However, for B3, when depth is larger than D4, it's very hard to judge whether there is a lump or not. Also, for B2, only when the depth is D1, the contrast is clear enough for human to judge. For D4, the smallest lump could be detected for sure is B5.

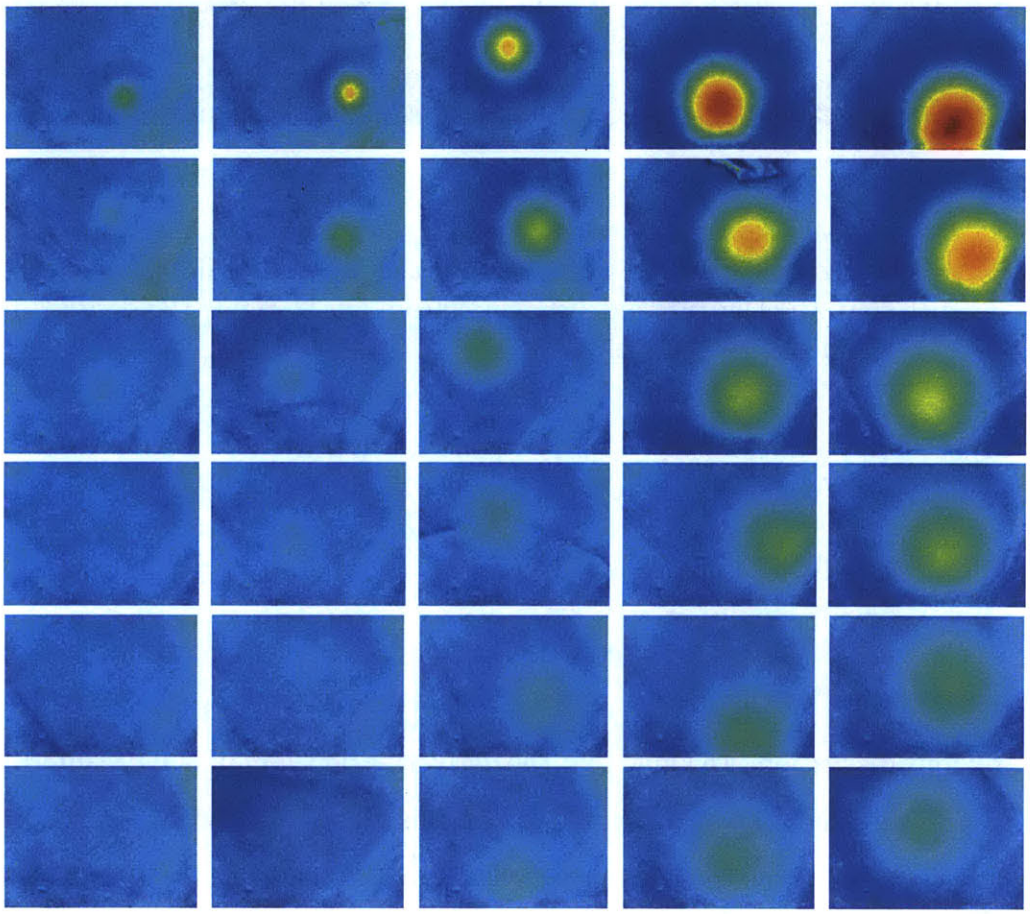

Figure 4-27: Derivative depth map of all H30-F4500 samples. Each row represent the samples with lump at different depth. From up to down, the depths are D1, D2, D3, D4, D5, D6, respectively. Each column represent the samples with lump of different sizes. From left to right, the sizes are B2, B3, B5, B8 and B9.5, respectively.

4.2.4 Computational Methodology for Lump Detection Using GelSight Sensor

As discussed in the previous session, just by looking at the depth map of different samples, the presence of the lump could be judged. However, if we feed computer with all the depth maps, how could the computer tell whether there is a lump in the sample. In this session, I will introduce a simple threshold method for lump detection.

1. From the original depth image, find the *mean* of the image.
2. Set a threshold for the "large" value. For example, $LargerValueThreshold = 1.5 \times mean$.
3. Find the number of pixels with value larger than the LargerValueThreshold, denoted as *num*.
4. Compute the ratio of *num* over the whole image, denoted as *ratio*
5. Set a threshold for the *RatioThreshold*. For example, $RatioThreshold = 0.14$
6. Compare *ratio* with *RatioThreshold* and give a binary feedback. If $ratio \geq RatioThreshold$, then there is a lump in the sample.

Using this method, some samples are selected for the experiment. As a comparison, the blank samples are used as the baseline to judge how well the method is for lump detection. For each sample, there are five trials, which means there are five data points for each sample.

4.2.4.1 Samples of different softness

Two samples with different softness are selected. They're H30-D3-B5 and H10-D3-B5. From Figure 4-28, the contrast for softer sample (b) is more obvious than the harder sample (a). From the data points for each sample, a normal distribution function is fitted. It's clear that the overlap of soft sample with soft blank sample is much smaller than the hard sample with hard blank sample.

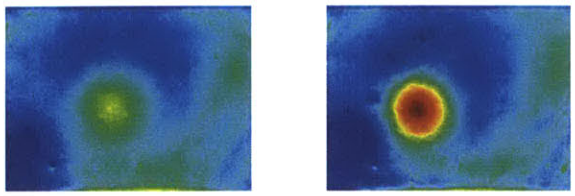

Figure 4-28: Depth map of samples with different softness. The left image shows the depth map of harder sample (H30-D3-B5), while the right image shows the depth map of softer sample (H10-D3-B5).

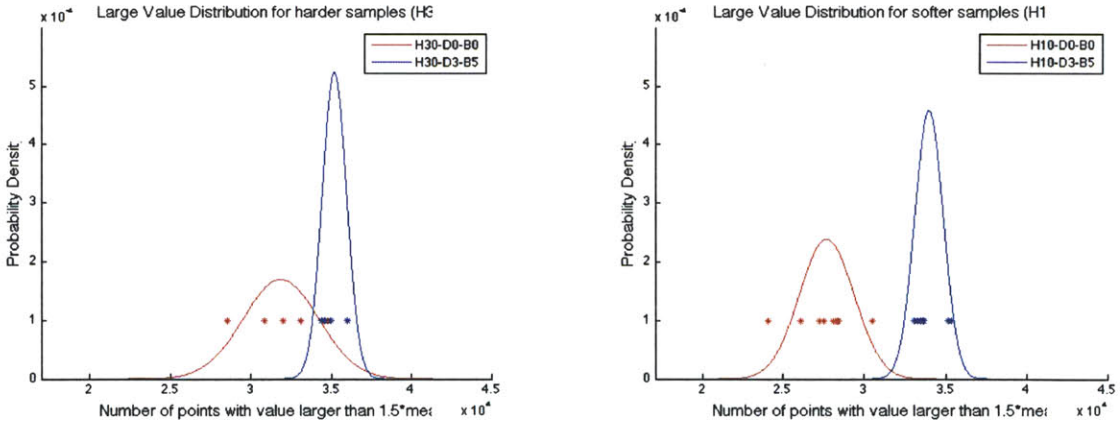

(a) (b)

Figure 4-29: Number of "large" value distribution for samples with different hardness. The red curve shows the distribution of blank sample with the same softness as the selected phantom sample. (a) is the distribution of harder sample (H30), (b) is the distribution of softer sample (H10).

To better visualize the overlap of the distribution functions, a ROC curve for both cases is plotted in Figure 4-30. From the ROC curve, it's clear that the d' for softer samples is larger than d' for harder samples, which means it's easier to tell the difference of lump presence in softer tissue rather than harder tissue It's intuitive that for soft phantoms samples, the contrast of the lump and the surrounding tissue larger, which is easier to tell the lump absence or presence.

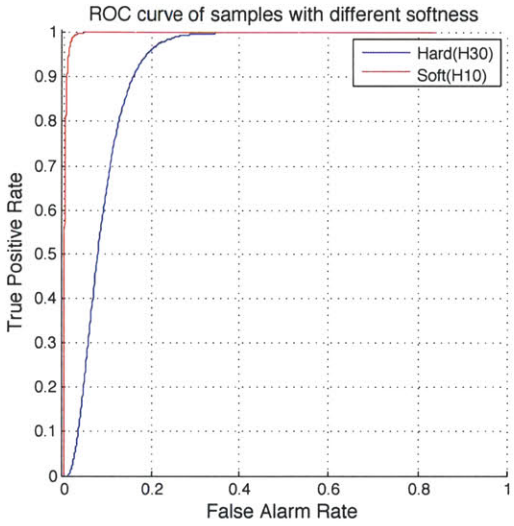

Figure 4-30: ROC curve for samples with soft tissue and hard tissue.

4.2.4.2 Samples with lump of different sizes

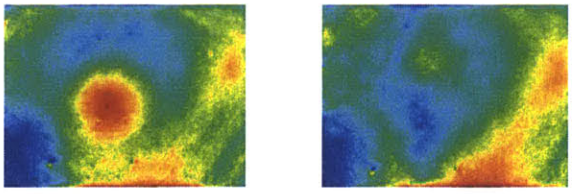

Figure 4-31: Depth map of samples with different lump sizes. The left image shows the depth map of sample with smaller lump (H30-D3-B3), while the right image shows the depth map of sample bigger lump (H30-D3-B5).

Two samples are selected, H30-D3-B3 and H30-D3-B5 shown in Figure 4-31. A normal distribution function of *num* is fitted for selected samples, shown in 4-32. To make it more clear, a ROC curve for both cases is plotted in Figure 4-33. From the

ROC curve, it's clear that the d' for sample with bigger lump is much larger than d' for sample with smaller lump, which means it's easier to tell the difference of lump presence or absence if the lump is bigger.

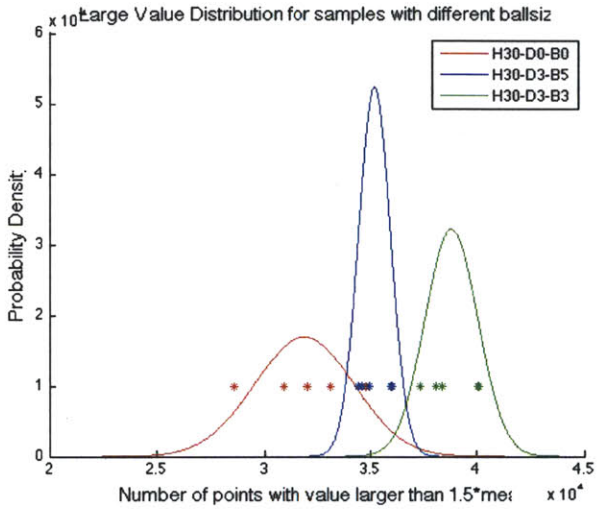

Figure 4-32: Number of "large" value distribution for samples with different sized lumps. The red curve shows the distribution of blank sample with the same softness as the selected phantom samples. The blue curve is the distribution of sample with bigger lump (H30-D3-B5), The green curve is the distribution of sample with smaller lump (H30-D3-B3).

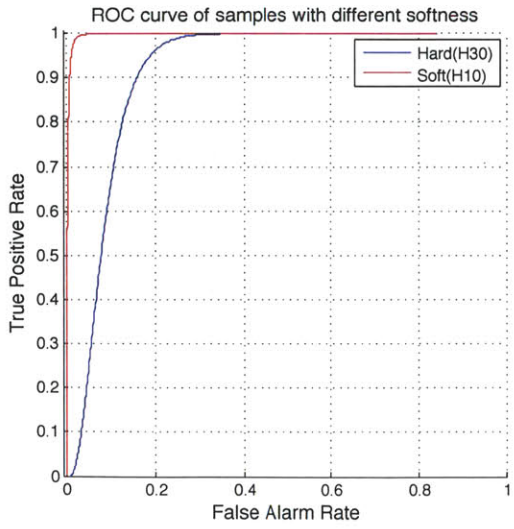

Figure 4-33: ROC curve for samples with different ballsize.

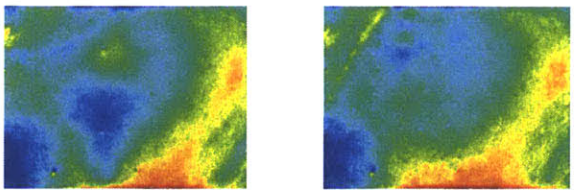

Figure 4-34: Depth map of samples with lump embedded at different depth. The left image shows the depth map of sample with lump embedded at a shallower position(H30-D3-B3), while the right image shows the depth map of sample with lump embedded at a deeper position (H30-D4-B3).

4.2.4.3 Samples with lump embedded at different depths

Two samples are selected, H30-D3-B3 and H30-D4-B3. The depth map for both samples are shown in Figure 4-34. The contrast are all not very clear, but there is still a small yellow circular region in **??**. A normal distribution function of *num* is fitted for selected samples, shown in 4-35.

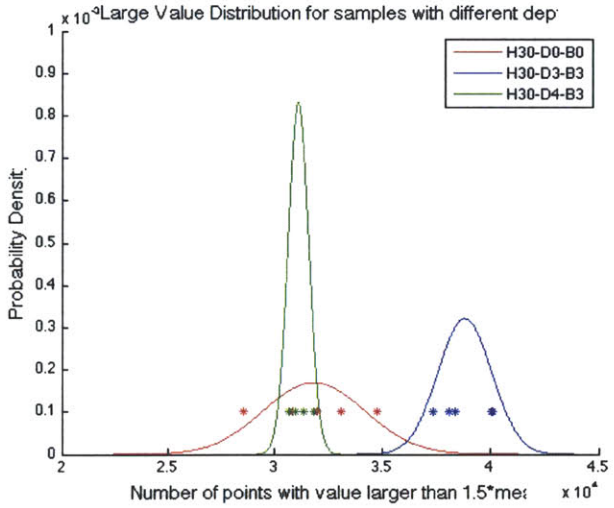

Figure 4-35: Number of "large" value distribution for samples with lump embedded at different depth. The red curve shows the distribution of blank sample with the same softness as the selected phantom samples. The blue curve is the distribution of sample with lump embedded at a shallower position (H30-D3-B3), The green curve is the distribution of sample with lump embedded at a deeper position (H30-D4-B3).

To make it more clear, a ROC curve for both cases is plotted in Figure 4-36. From the ROC curve, it's clear that the d' for sample with lump embedded at a shallower position is much larger than d' for sample with lump embedded at a deeper position,

which means it's easier to tell whether there is lump embedded in the tissue if the lump is close to the surface.

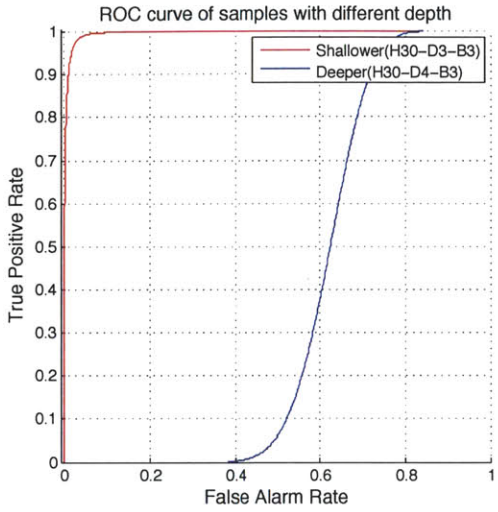

Figure 4-36: ROC curve for samples with ball embedded at different depths

4.2.4.4 Samples with different force applied

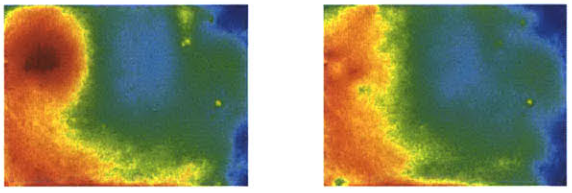

Figure 4-37: Depth map of the same sample (H10-D6-B5) applied by different forces. The left image shows the depth map of the sample pressed with larger force, while the right image shows the depth map of the sample pressed by smaller force

I'm testing the same sample with different forces. H10-D6-B5 is selected. The depth map for both cases are shown in Figure 4-37. The contrast are all not so obvious, but it's clear that there is a small red circular region in **??**. A normal distribution function of *num* is fitted for selected samples, shown in 4-38. There is overlap of phantom sample distribution and the blank sample distribution in while a small force is applied. While when the force increased, the overlap between the phantom sample distribution and the blank sample distribution disappears. In ROC

curve shown in Figure 4-39, d' for sample with larger force applied is much larger than d' for sample with smaller force applied, which means it's easier to tell the difference of lump presence or absence when more force is applied.

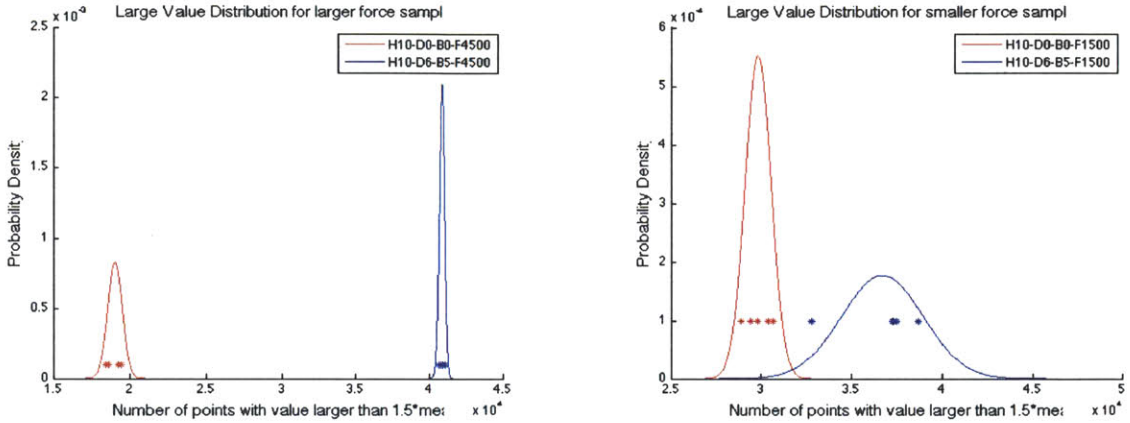

(a) (b)

Figure 4-38: Number of "large" value distribution for the same sample while different forces are applied. The red curve shows the distribution of blank sample with the same force applied as the phantom sample. (a) is the distribution of the sample with larger force, (b) is the distribution of the sample with smaller force.

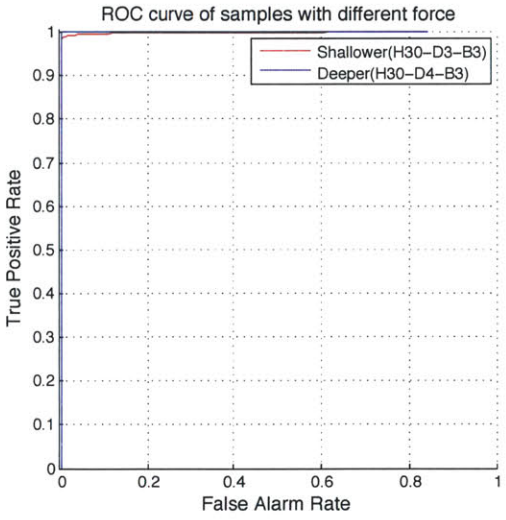

Figure 4-39: ROC curve for sample while applied different amount of force.

4.2.4.5 Result of Lump Detection Using Threshold method

From all the depth map of different samples, the binary result could be gained by a simple threshold method. The *RatioThreshold* could be adjusted according to the tolerance of false alarm. Any sample that could satisfy $ratio \geq RatioThreshold$ will be labeled as "lump presence".

When $RatioThreshold = 0.14$, all the 60 phantom samples with lumps and 10 blank samples (five for each softness) are tested. This threshold could prevent the false alarms. The detection result for all the phantom samples are shown in 4-40, which could match up with the depth image shown in 4-27. For all the H30 samples, the deepest depth for B3 samples that could be detected by this method is D3, and the smallest lump that could be detected of D6 samples is B5.

	00-10 (H10)					00-30 (H30)				
(mm)	B1	B2	B3	B4	B5	B1	B2	B3	B4	B5
	2	3	5	8	9.5	2	3	5	8	9.5
D1	1	1	1	1	1	1	1	1	1	1
D2	2	2	2	2	2	2	2	2	2	2
D3	3	3	3	3	3	3	3	3	3	3
D4	4	4	4	4	4	4	4	4	4	4
D5	5	5	5	5	5	5	5	5	5	5
D6	6	6	6	6	6	6	6	6	6	6

Figure 4-40: Lump Detection Result of all samples with 2 softness, 6 depths, 5 ballsizes. The yellow part indicate that the sample could be detected with high confidence.

There are still some issues with this method. The ratio threshold is set to prevent false alarms, while in real medical examinations, doctors tend to not miss any possible target and not avoid false alarm.

From all the experiment of lump detection using GelSight sensor, we know that softness of the tissue, size of the lump, the depth of the lump embedded in the tissue and the force applied on the sample, all factors that could influence the detection result.

4.3 Human Psychological Experiment in Lump Detection

4.3.1 Human Experiment Setup

The purpose of this task is to see how human performs in the lump detection tasks. Human subjects could have bias while doing this experiments. For example, by choosing one of two samples, there will be 50% correction rate simply by guessing. To make human subject experiment result more reliable, we adapt two-alternative forced choice (2AFC) method. 2AFC task is a psychophysical method for eliciting responses from a person about his or her experiences of a stimulus. Specifically, the 2AFC experimental design is commonly used to test speed and accuracy of choices between two alternatives given a timed interval [149].

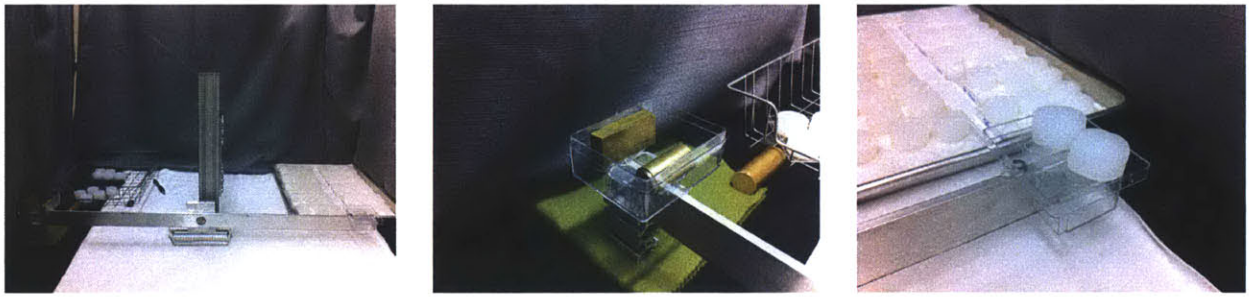

(a) (b) (c)

Figure 4-41: Setup for the human subject experiment.

In this experiment, the phantom used in lump detection of GelSight sensor is also used as stimuli for human psychological experiment. As shown in Figure 4-41 a, a long arm balance is used to control the maximum force the subject could apply to the phantom samples. At one end of the balance (shown in Figure 4-41 b), metal blocks with known weight are placed to control the maximum force. At the other end (shown in Figure 4-41 c), two samples, one with lump and one without, are presented to the subject. During the experiment, the subject could freely observe the phantom using one finger. For each trial, the subject is given 12 seconds to explore just by tactile

sensation. At the end of each trial, the subject is asked to point out the phantom sample with lump embedded. For each pair, 40 trails are conducted, which means there are 40 data points for each sample.

4.3.2 Human Experiment Methodology and Result

For five phantom samples of H30-D3, the probability of correct response is shown in Figure 4-42. From the figure, to get 75% correct response, the lump size is 4 mm. For six phantom samples of H30-B5, the probability of correct response is shown in Figure 4-43 . From the figure, to get 75% correct response, the depth is 5.1 mm. To map the human performance result to all the H3 samples, we could know that human could detect lumps bigger than B5 for D3 samples, and D5 for B3 samples.

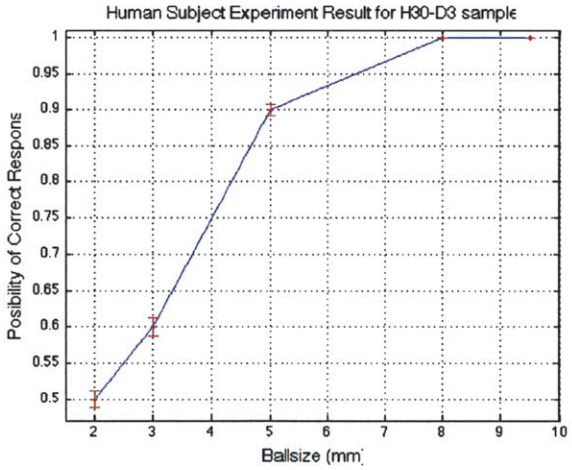

Figure 4-42: Probability of correct response

4.4 Conclusion

For H30 samples, the deepest depth for GelSight sensor to B3 samples is D3, and the smallest lump for GelSight sensor to detect for D6 samples is B5. For human performance, human could detect lumps bigger than B5 for D3 samples, and D5 for B3 samples. Mapping performance of human subjects and GelSight performance to al the H30 samples, the result is shown in figure 4-44. GelSight Sensor outperforms

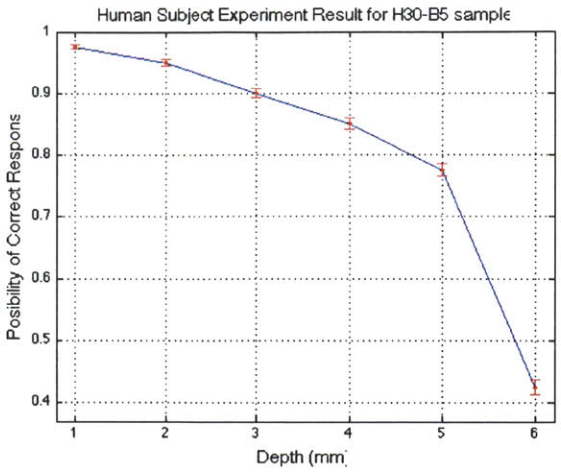

Figure 4-43: Probability of correct response

human in lump detection task.

	Human Performance (H30)					Sensor Performance (H30)				
(mm)	B1	B2	B3	B4	B5	B1	B2	B3	B4	B5
	2	3	5	8	9.5	2	3	5	8	9.5
D1	1	1	1	1	1	1	1	1	1	1
D2	2	2	2	2	2	2	2	2	2	2
D3	3	3	3	3	3	3	3	3	3	3
D4	4	4	4	4	4	4	4	4	4	4
D5	5	5	5	5	5	5	5	5	5	5
D6	6	6	6	6	6	6	6	6	6	6

Figure 4-44: Comparison of human performance and GelSight sensor performance in lump detection experiment

There are still some remaining issues for this experiment. First is that the mechanical properties of phantom samples are changing as more history added to the sample, which makes the data noisy. Second, the setup of GelSight sensor experiment is not ideal, which will bring in some noise to the data. Third, there are only five data points for each sample in GelSight sensor experiment. Fourth is how to display the tactile information to the user. It might be more useful for the user to have a possibility of lump presence rather than just having binary detection result.

Chapter 5

Conclusion and Future Work

5.1 Conclusion

GelSight sensor is a novel tactile sensor for measuring surface geometry, from which a lot of information could be inferred. In this thesis, I implemented GelSight principle to reconstruct surface geometry, based on which, the roughness comparison and lump detection experiment are conducted. For lump detection experiment, a Also, by using Instron Indentation machine, softness of different samples is detected. The indentation experiment of GelSight sensor also shows the history of the sensor will influence sensor's mechanical property. Below is the list of my work for this thesis.

1 Implement photometric stereo algorithm to reconstruct surface geometry.

2 Roughness comparison of sandpaper samples.

3 Softness detection of different rubber samples.

4 Mechanical properties of the sensor will change over time of usage.

5 Lump Detection using GelSight sensor is promising

6 Human subject experiment for lump detection as a comparison of sensor performance.

5.2 Future Work

Even though GelSight sensor principle seems simple, it still needs a lot of work for any specific application. I did some improvement of illumination and sensor shape in the past, but there is no good result yet. I will keep working on the device design in the future. Also, lump detection is a great application. It will make a difference for medical industry of GelSight sensor finally is applied in lump detection. Here is the list of things I will do in the future.

1 Build the dome shape sensor and figure out the illumination for it.

2 Scale down current GelSight sensor devices to implement sensor in robotic finger.

3 Measure mechanical property of GelSight sensor.

4 Infer force information from depth map using finite element method.

5 Connect GelSight data with physical unit.

6 Conduct more experiment in lump detection including sensor experiment and human psychological experiment.

Bibliography

[1] Astm-d-1415: Plastic test standard - international rubber hardness degrees (irhd).

[2] Astm-d-2204: Method of test for perspiration resistance of organic coatings.

[3] Iso-868: Shore hardness.

[4] Test method of metallic materials brinell hardness test.

[5] *Equotip Metal Hardness*, 2008.

[6] Basic durometer testing information, 2011.

[7] S. Ando and H. Shinoda. Ultrasonic emission tactile sensing. *Control Systems, IEEE*, 15(1):61 –69, feb 1995.

[8] Apple. Itouch commercial website.

[9] H. Athenstaedt, H. Claussen, and D. Schaper. Epidermis of human skin: pyroelectric and piezoelectric sensor layer. *Science*, 216:1018–1020, 1982.

[10] A. S. Augurelle, A. M. Smith, T. Lejeune, and J. L. Thonnard. Importance of cutaneous feedback in maintaining a secure grip during manipulation of hand-held objects. *J. Neurophsiol.*, 89:665–671, 2003.

[11] P. R. Basu, R. A. Russell, and G. Trott. Extracting 3-dimensional surface features from tactile data. In *Int. Symp. Expo. Robots*, pages 908–920, Sydney, Australia, 1988.

[12] David J. Beebe, Arthur S. Hsieh, Denice D. Denton, and Robert G. Radwin. A silicon force sensor for robotics and medicine. *Sensors and Actuators A: Physical*, 50(12):55 – 65, 1995.

[13] R. J. V. Beers and D. M. Wolpert. When feeling is more important than seeing in sensorimotor adaptation. *Curr. Biol.*, 12:834–837, 2002.

[14] Jean M. Bennett and Lars Mattsson. *Introduction to surface roughness and scattering.* Optical Society of America, Washington, D.C, 2nd edition, 1999.

[15] S. J. Bensmaia, J. C. Craig, and K. O. Johanson. Temporal factors in tactile spatial acuity: Evidence for ra interference in fine spatial processing. *J. Neurophsiol.*, 95:1783–1791, 2006.

[16] A. D. Berger and P. K. Khosla. Using tactile data for real-time feedback. *Int. J. Robot. Res.*, 10(2):88–102, 1991.

[17] A. Berthoz. *The Brain's Sense of Movement.* Harvard Univ. Press, Cambridge, MA/London, U.K, 2000.

[18] A. Bicchi, J. K. Salisbury, and P. Dario. Augmentation of grasp ro- bustness using intrinsic tactile sensing. In *IEEE Int. Conf. Robot. Autom.*, pages 302–307, AZ, May 1989.

[19] F. Binkofski, E. Kunesch, J. Classen, R. J. Seitz, and H. J. Freund. Tactile apraxia—unimodal apractic disorder of tactile object recognition associated with parietal lobe lesions. *Brain*, 124:132–144, 2001.

[20] I. Birznieks, P. Jenmalm, A. W. Goodwin, and R. S. Johannson. Encoding of direction of fingertip forces by human tactile afferents. *J. Neurosci.*, 21:8222–8237, 2001.

[21] CALCE and the University of Maryland, editors. *Material Hardness.* 2001.

[22] C. J. Cascio and K. Sathian. Temporal cues contribute to tactile per- ception of roughness. *J. Neurosci.*, 21:5289–5296, 2001.

[23] N. Cauna. Nature and functions of the papillary ridges of the digital skin. *Anat. Record*, 119:449–468, 1954.

[24] M. Charlebois, K. Gupta, and S. Payandeh. On estimating local shape using contact sensing. *J. Robot. Syst.*, 17:643–658, 2000.

[25] Hsiupei Chen, Tim J. Lamer, Richard H. Rho, Kenneth A. Marshall, B. Todd Sitzman, Salim M. Ghazi, and Randall P. Brewer. Contemporary management of neuropathic pain for the primary care physician. *Mayo Clinic Proceedings*, 79(12):1533 – 1545, 2004.

[26] Edward Cheung and Vladimir J. Lumelsky. A sensitive skin system for motion control of robot arm manipulators. *Robotics and Autonomous Systems*, 10(1):9–32, 1992.

[27] Byung-June Choi, Sung-Chul Kang, and Hyouk-Ryeol Choi. *Development of tactile sensor for detecting contact force and slip*, volume 30, pages 2638–2643. IEEE, 2005.

[28] Z. Chu, P. M. Sarro, and S. Middelhoek. Silicon three-axial tactile sensor. *Sens. Actuators A*, 54:505–510, 1996.

[29] Z. Chu, P.M. Sarro, and S. Middelhoek. Silicon three-axial tactile sensor. In *Solid-State Sensors and Actuators, 1995 and Eurosensors IX.. Transducers '95. The 8th International Conference on*, volume 1, pages 656 –659, jun 1995.

[30] Shadow Robot Co. Design of a dextrous hand for advanced clawar applications. *Climbing and Walking Robots and the Supporting Technologies for Mobile Machines*, pages 691–698, 2003.

[31] Shadow Robot Co. Developments in dextrous hands for advanced robotic applications. In *Automation Congress, 2004. Proceedings. World*, volume 15, pages 123 –128, 28 2004-july 1 2004.

[32] J. C. Craig. Grating orientation as a measure of tactile spatial acuity. *Somatosens. Motor Res.*, 16:197–206, 1999.

[33] J. C. Craig and X. Baihua. Temporal order and tactile patterns. *Percept. Phychophys.*, 47:22–34, 1990.

[34] J. C. Craig and J. M. Kisner. Factors affecting tactile spatial acuity. *Somatosens. Motor Res.*, 1:29–45, 1998.

[35] J. C. Craig and K. B. Lyle. A comparison of tactile spatial sensitivity on the palm and fingerpad. *Percept. Phychophys.*, 63:337–347, 2001.

[36] R. M. Crowder. Toward robots that can sense texture by touch. *Science*, 312:1478–1479, 2006.

[37] R.M Crowder. Tactile sensing. January 1998.

[38] M. R. Cutkosky and I. Kao. Computing and controlling the compliance of a robotic hand. *IEEE Trans. Robot. Autom.*, 5(2):151–165, 1989.

[39] R.S. Dahiya, G. Metta, M. Valle, and G. Sandini. Tactile sensing – from humans to humanoids. *Robotics, IEEE Transactions on*, 26(1):1 –20, feb. 2010.

[40] R.S. Dahiya, M. Valle, G. Metta, and L. Lorenzelli. Posfet based tactile sensor arrays. In *Electronics, Circuits and Systems, 2007. ICECS 2007. 14th IEEE International Conference on*, pages 1075 –1078, dec. 2007.

[41] R.S. Dahiya, M. Valle, G. Metta, and L. Lorenzelli. Spice model of lossy piezoelectric polymers. In *Applications of Ferroelectrics, 2008. ISAF 2008. 17th IEEE International Symposium on the*, volume 3, pages 1 –4, feb. 2008.

[42] K. Dandekar, B. I. Raju, and M. A. Srinivasan. 3-d finite-element- models of human and monkey fingertips to investigate the mechanics of tactile sensing. *J. Biomech. Eng.*, 125(5):682–691, 2003.

[43] J Dargahi, M Parameswaran, and S Payandeh. A micromachined piezoelectric tactile sensor for an endoscopic grasper-theory, fabrication and experiments, 2000.

[44] P. Dario. Tactile sensing: Technology and applications. *Sensors and Actuators A: Physical*, 26(13):251 – 256, 1991. ¡ce:title¿Proceedings of Eurosensors IV held in jointly with Sensoren Technologies und Anwendung¡/ce:title¿.

[45] P. Dario and D. de Rossi. Tactile sensors and gripping challenge. *IEEE Spectrum,*, 22(8):46–52, August 1985.

[46] R.J. De Souza and K.D. Wise. A very high density bulk micromachined capacitive tactile imager. In *Solid State Sensors and Actuators, 1997. TRANSDUCERS '97 Chicago., 1997 International Conference on*, volume 2, pages 1473 –1476 vol.2, jun 1997.

[47] E. Paul Degarmo, J T. Black, and Ronald A Kohser, editors. *Materials and Processes in Manufacturing.* 9th edition, 2003.

[48] Analog Device. Data sheet ad 7147: Captouch programmable controller for single-electrode capacitance sensors.

[49] M.A. Diftler, C.J. Culbert, R.O. Ambrose, Jr. Platt, R., and W.J. Bluethmann. Evolution of the nasa/darpa robonaut control system. In *Robotics and Automation, 2003. Proceedings. ICRA '03. IEEE International Conference on*, volume 2, pages 2543 – 2548 vol.2, sept. 2003.

[50] C. Domenici, D. D. Rossi, A. Bicchi, and S. Bennati. Shear stress detection in an elastic layer by a piezoelectric polymer tactile sensor. *IEEE Trans. Electr. Insulation*, 24(6):1077–1081, 1989.

[51] Interlink Electronics. Tactile sensor commercial website.

[52] R. E. Ellis and M. Qin. Singular-value and finite-element analysis of tactile shape recognition. In *IEEE Int. Conf. Robot. Autom.*, pages 2529–2535, San Diego, CA, May 1994.

[53] B. F. V. Erp. Vibrotactile spatial acuity on the torso: effect of location and timing parameters. In *1st Joint Eurohaptics Conf. Haptic Interfaces Virtual Environ*, 2005.

[54] J. B. Fallon and D. L. Morgan. Fully tuneable stochastic resonance in cutaneous receptors. *J. Neurophsio.*, 94:928–933, 2005.

[55] R. S. Fearing. Tactile sensing mechanisms. *Int. J. Robot. Res.*, 9(3):3–23, 1990.

[56] R.S. Fearing and T.O. Binford. Using a cylindrical tactile sensor for determining curvature. *Robotics and Automation, IEEE Transactions on*, 7(6):806 –817, dec 1991.

[57] J. R. Flanagan and A. M. Wing. Modulation of grip force with load force during point-to-point arm movements. *Exp. Brain Res.*, 95:131–143, 1993.

[58] G. J. Gerling and G. W. Thomas. The effect of fingertip mircostructures on tactile edge perception. In *First Joint Eurohaptics Conf. Symp. Haptic Interfaces Virtual Environ. Teleoperator Syst.*, pages 63–72, 2005.

[59] G. J. Gerling and G. W. Thomas. Fingerprint lines may not directly affect sa i mechanoreceptor response. *Somatosens. Motor Res.*, 25:61–76, 2008.

[60] A. W. Goodwin, V. G. Macefield, and J. W. Bisley. Encoding of object curvature by tactile afferents from human fingers. *J. Neurophsiol.*, 78:2881–2888, 1997.

[61] A. M. Gordon, H. Forssberg, R. S. Johansson, and G. Westling. The integration of haptically acquired size information in the programming of precision grip. *Exp. Brain Res.*, 83:483–488, 1991.

[62] A. M. Gordon, H. Forssberg, R. S. Johansson, and G. Westling. Integration of sensory information during the programming of precision grip: comments on the contributions of size cues. *Exp. Brain Res.*, 85:226–229, 1991.

[63] B.L. Gray and R.S. Fearing. A surface micromachined microtactile sensor array. In *Robotics and Automation, 1996. Proceedings., 1996 IEEE International Conference on*, volume 1, pages 1 –6 vol.1, apr 1996.

[64] M. S. A. Graziano, M. M. Botvinick W. Prinz, and B. Hommel. *Common Mechanisms in Perception and Action: Attention and Performance*, page 136. Oxford Univ. Press, 2002.

[65] J.C. Gwilliam, Z. Pezzementi, E. Jantho, A.M. Okamura, and S. Hsiao. Human vs. robotic tactile sensing: Detecting lumps in soft tissue. In *Haptics Symposium, 2010 IEEE*, pages 21 –28, march 2010.

[66] Y. Hasegawa, T. Shimizu, T. Miyaji, M. Shikida, H. Sasaki, K. Sato, and K. Itoigawa. Hardness detection using a micromachined active tactile sensor. In *TRANSDUCERS, Solid-State Sensors, Actuators and Microsystems, 12th International Conference on, 2003*, volume 1, pages 927 – 930 vol.1, june 2003.

[67] Jin-Seok Heo, Jong-Ha Chung, and Jung-Ju Lee. Tactile sensor arrays using fiber bragg grating sensors. *Sensors and Actuators A: Physical*, 126(2):312 – 327, 2006.

[68] K. Hosoda, Y. Tada, and M. Asada. Anthropomorphic robotic soft fin- gertip with randomly distributed receptors. *Robot. Auton. Syst.*, 54(2):104–109, 2006.

[69] R. D. Howe. Tactile sensing and control of robotic manipulation. *J. Adv. Robot.*, 8:245–261, 1994.

[70] R. D. Howe and M. R. Cutkosky. Sensing skin acceleration for slip and texture perception. In *IEEE Int. Conf. Robot. Autom.*, pages 145–150, Scottsdale, AZ, 1989.

[71] R. D. Howe and M. R. Cutkosky. Integrating tactile sensing with control for dextrous manipulation. In *IEEE Int. Workshop Intell. Motion Control*, volume 1, pages 369–374, Istanbul, Turkey,, August 1990.

[72] R. D. Howe and M. R. Cutkosky. Dynamic tactile sensing: Perception of fine surface features with stress rate sensing. *IEEE Trans. Robot. Autom.*, 2(2):140–151, April 1993.

[73] K. Hoyt, B. Castaneda, M. Zhang, P. Nigwekar, P. A. DiSantagnese, J. V. Joseph, J. Strang, D. J. Rubens, and K. J. Parker. Tissue elasticity properties as biomarkers for prostate cancer. *Cancer Biomarkers*, 4(4-5):213–225, 2008.

[74] AMETEX Inc. Hardness tester commercial website.

[75] Pressure Profile Systems Inc. Robotouch sensor commercial website.

[76] Ville Jalkanen, Britt Andersson, Anders Bergh, Brje Ljungberg, and Olof Lindahl. Prostate tissue stiffness as measured with a resonance sensor system: a study on silicone and human prostate tissue in vitro. *Medical and Biological Engineering and Computing*, 44:593–603, 2006. 10.1007/s11517-006-0069-6.

[77] L. Jamone, G. Metta, F. Nori, and G. Sandini. James: A humanoid robot acting over an unstructured world. In *Humanoid Robots, 2006 6th IEEE-RAS International Conference on*, pages 143 –150, dec. 2006.

[78] B. V. Jayawant. Tactile sensing in robotics. *J. Phys. E: Sci. Instrum.*, 22:684, 1989.

[79] P. Jenmalm, I. Birznieks, A. W. Goodwin, and R. S. Johannson. In- fluence of object shape on responses of human tactile afferents under conditions characteristics of manipulation. *Eur. J. Neurosci.*, 18:164–176, 2003.

[80] K. O. Johannson and J. R. Phillips. Tactile spatial resolution. i. two-point discrimination, gap detection, grating resolution, and letter recognition. *J. Neurophsiol.*, 46:1177–1192, 1981.

[81] R. S. Johannson and J. R. Flanagan. Coding and use of tactile signals from the fingertips in object manipulation tasks. *Nature Rev. Neurosci.*, Advance Online Publication:1, 2009.

[82] R. S. Johannson and A. B. Vallbo. Tactile sensibility in the human hand: Relative and absolute densities of four types of mechanoreceptive units in glabrous skin. *J. Physio.*, 286:283–300, 1979.

[83] R S Johansson, U Landstrm, and R Lundstrm. Responses of mechanoreceptive afferent units in the glabrous skin of the human hand to sinusoidal skin displacements. *Brain Research*, 244(1):17–25, 1982.

[84] R. S. Johansson and G. Westling. Roles of glabrous skin receptors and sensorimotor memory in automatic control of precision grip when lifting rougher or more slippery objects. *Exp. Brain Res.*, 56:550–564, 1984.

[85] Roland S Johansson and Ingvars Birznieks. First spikes in ensembles of human tactile afferents code complex spatial fingertip events. *Nat Neurosci*, 7(2):170–177, 02 2004.

[86] K. O. Johnson and S. S. Hsiao. Neural mechanisms of tactual form and texture perception. *Annu. Rev. Neurosci.*, 15:227–250, 1992.

[87] Micah K. Johnson and Edward H. Adelson. Retrographic sensing for the measurement of surface texture and shape. In *Computer Vision and Pattern Recognition (CVPR)*, pages 1070–1077, 2009.

[88] Micah K. Johnson, Forrester Cole, Alvin Raj, and Edward H. Adelson. Microgeometry capture using an elastomeric sensor. *ACM Transactions on Graphics (Proc. ACM SIGGRAPH)*, 30(4):461–468, 2011.

[89] L. A. Jones and S. J. Lederman. *Human Hand Function*, chapter Tactile sensing, pages 44–74. Cambridge, MA: Oxford Univ. Press, 2006.

[90] L. A. Jones and E. Piateski. Contribution of tactile feedback from the hand to the perception of force. *Exp. Brain Res.*, 168:298–302, 2006.

[91] J. H. Kaas. The functional organization of somatosensory cortex in primates. *Ann Anat*, 175:509–518, 1993.

[92] E. R. Kandel, J. H. Schwartz, and T. M. Jessell. *Principles of Neural Science, 4th ed.* New York: McGraw-Hill Medical, 2000.

[93] P. S. Khalsa, R. M. Friedman, M. A. Srinivasan, and R. H. LaMotte. Encoding of shape and orientation of objects indented into the monkey fingerpad by populations of slowly and rapidly adapting mechanorecep- tors. *J. Neurophsiol.*, 79:3238–3251, 1998.

[94] R. Kikuuwe, A. Sano, H. Mochiyama, N. Takesue, and H. Fujimoto. A tactile sensor capable of mechanical adaptation and its use as a surface deflection detector. In *IEEE Sens.*, pages 256–259, 2004.

[95] S. L. Kilbreath, K. Refshauge, and S. C. Gandevia. Differential control of digits in human hand: Evidence from digital anaesthesia and weight matching. *Exp. Brain Res.*, 117:507–511, 1997.

[96] E. Daniel Kirby, Zhe Zhang, and Joseph C. Chen. Development of an accelerometer-based surface roughness prediction system in turning operations using multiple regression techniques. *National Association of Industrial Technology*, 20(4), 2004.

[97] E. M. Kirkpatrick, editor. *Chambers 20th Century Dictionary.* Edinburgh: W & R Chambers Ltd., 1983.

[98] R. L. Klatzky, S. J. Lederman A. F. Healy, and R. W. Proctor. Touch. *Experimental Psychology*, 4:147, 2003.

[99] R. L. Klatzky, S. J. Lederman, and V. A. Metzger. Identifying objects by touch: An 'expert system. *Percept. Psychophys.*, 37:299–302, 1985.

[100] F. Knoop, C.G. Peters, and W.B. Emerson. A sensitive pyramidal-diamond tool for indentation measurements. *Journal of Research of the National Bureau of Standards*, 23:39–6', 1939.

[101] Edward S. Kolesar, Rocky R. Reston, Douglas G. Ford, and Robert C. Fitch. Multiplexed piezoelectric polymer tactile sensor. *Journal of Robotic Systems*, 9(1):37–63, 1992.

[102] E.S. Kolesar, C.S. Dyson, R.R. Reston, R.C. Fitch, D.G. Ford, and S.D. Nelms. Tactile integrated circuit sensor realized with a piezoelectric polymer. In *Innovative Systems in Silicon, 1996. Proceedings., Eighth Annual IEEE International Conference on*, pages 372 –381, oct 1996.

[103] G.M. Krishna and K. Rajanna. Tactile sensor based on piezoelectric resonance. In *Sensors, 2002. Proceedings of IEEE*, volume 2, pages 1643 – 1647 vol.2, 2002.

[104] T. Krouskop, T. Wheeler, F. Kallel, and B. Garra. Elastic moduli of breast and prostate tissues under compression. *Ultrasonic imaging*, 20(4):260–274, December 1998.

[105] T. A. Krouskop, T. M. Wheeler, F. Kallel, B. S. Garra, and T. Hall. Elastic moduli of breast and prostate tissues under compression. *Ultrasonic Imaging*, 20(4):260–274, 1998.

[106] National Physical Laboratory. *Rubber Hardness.* 2006.

[107] R. H. LaMotte and M. A. Srinivasan. Tactile discrimination of shape: Responses of slowly adapting mechanoreceptive afferents to a step stroked across the monkey fingerpad. *J. Neurosc.*, 7:1655–1671, 1987.

[108] S. J. Lederman. Heightening tactile impressions of surface texture. In *Active Touch: The Mechanicsm of Recognition of Objects by Manipula- tion. An Interdisciplinary Approach.* G. Gordon, Ed., 1978.

[109] S. J. Lederman. The perception of surface roughness by active and passive touch. *Bull. Psychon. Soc.*, 18:253–255, 1981.

[110] S. J. Lederman and D. T. Pawluk. Lessons from the study of biological touch for robotic tactile sensing. In H. R. Nicholls, editor, *Advanced Tactile Sensing for Robots, ser. Robotics and Automated Systems*, volume 5, pages 151–192, Singapore, 1992. World Scientific.

[111] Susan J. Lederman and Roberta L. Klatzky. Sensing and displaying spatially distributed fingertip forces in haptic interfaces for teleoperator and virtual environment systems. *Presence: Teleoper. Virtual Environ.*, 8(1):86–103, February 1999.

[112] M H Lee. Tactile sensing: New directions, new challenges. *The International Journal of Robotics Research*, 19(7):636–643, 2000.

[113] M. H. Lee and H. R. Nicholls. Tactile sensing for mechatronics - a state of the art survey. *Mechatron.*, 9:1–31, 1999.

[114] Z. Li, P. Hsu, and S. Sastry. Grasping and coordinated manipulation by a multifingered robot hand. *Int. J. Robot. Res.*, 8(4):33–50, 1989.

[115] J. M. Loomis and S. J. Lederman. Cognitive processes performances. *Tactual Perceptio (vol. 2, Handbook of Perception and Human Perfor- mances Series).*, 2, 1986.

[116] H. Maekawa, K. Tanie, K. Komoriya, M. Kaneko, C. Horiguchi, and T. Sugawara. Development of a finger-shaped tactile sensor and its evaluation by active touch. In *Robotics and Automation, 1992. Proceedings., 1992 IEEE International Conference on*, pages 1327 –1334 vol.2, may 1992.

[117] T. Maeno, T. Kawamura, and S. Cheng. Friction estimation by pressing an elastic finger-shaped sensor against a surface. *IEEE Trans. Robot. Autom.*, 20(2):222–228, April 2004.

[118] T. Maeno, K. Kobayashi, and N. Yamazaki. Relationship between the structure of human finger tissue and the location of tactile receptors. *Bull. JSME Int. J.*, 41:94–100, 1998.

[119] M. Maggiali, G. Cannata, P. Maiolino, G. Metta, M. Randazzao, and G. Sandini. Embedded tactile sensor modules. In *11th Mechatron. Forum Biennial Int. Conf.*, Limerick, Ireland, 2008.

[120] V. Maheshwari and R. F. Saraf. High-resolution thin-film device to sense texture by touch. *Science*, 312:1501–1504, 2006.

[121] McMasterCarr. Mcmastercarr commercial website for sandpaper.

[122] E. M. Meftah, L. Belingard, and C. E. Chapman. Relative effects of the spatial and temporal characteristics of scanned surfaces on human perception of tactile roughness using passive touch. *Exp. Brain Res.*, 132:351–361, 2000.

[123] S. Miyazaki and A. Ishida. Capacitive transducer for continuous measurement of vertical foot force. *Medical and Biological Engineering and Computing*, 22:309–316, 1984. 10.1007/BF02442098.

[124] M. Molina and F. Jouen. Manual cyclical activity as an exploratory tool in neonates. *Infant Behavior and Development*, 27:42–53, 2004.

[125] J. W. Morley, A. W. Goodwin, and I. Darian-Smith. Tactile discrimina- tion of gratings. *Exp. Brain Res.*, 49:291–299, 1983.

[126] R. M. Murray, Z. Li, and S. S. Sastry. *A Mathematical Introduction to Robotic Manipulation.* CRC, FL, 1st edition, 1994.

[127] K. Nakamura and H. Shinoda. A tactile sensor instantaneously evaluating friction coefficients. In *TRANSDUCERS 1997 Int. Conf. Solid-State Sens. Actuators*, pages 1430–1433, 2001.

[128] T. Nelson, R. vanDover, S. Jin, S. Hackwood, and G. Beni. Shear-sensitive magnetoresistive robotic tactile sensor. *Magnetics, IEEE Transactions on*, 22(5):394 – 396, sep 1986.

[129] J. L. Novak. Initial design and analysis of a capacitive sensor for shear and normal force measurement. In *IEEE Int. Conf. Robot. Autom.*, pages 137–145, Scottsdale, AZ, 1989.

[130] M. Ohka, H. Kobayashi, J. Takata, and Y. Mitsuya. Sensing precision of an optical three-axis tactile sensor for a robotic finger. In *Robot and Human Interactive Communication, 2006. ROMAN 2006. The 15th IEEE International Symposium on*, pages 214 –219, sept. 2006.

[131] Yoshiyuki Ohmura, Yasuo Kuniyoshi, and Akihiko Nagakubo. Conformable and scalable tactile sensor skin for curved surfaces. In *ICRA*, pages 1348–1353. IEEE, 2006.

[132] S. Omata, Y. Murayama, and C. E. Constantinou. Real time robotic tactile system for development of the physical properties of biomaterials. *Sens. Actuators A*, 112:278–285, 2004.

[133] W. Peine and R. Howe. Do humans sense finger deformation or distributed pressure to detect lumps in soft tissue? *ASME Dynamic Systems and Control Division*, pages 273–278, 1998.

[134] Peratech. Quantum tunnel tactile sensor commercial website.

[135] J. R. Phillips and K. O. Johnson. Tactile spatial resolution iii —a continuum mechacnics model of skin predicting mechanoreceptors re- sponses to bars, edges, and gratings. *J. Neurophsiol.*, 46:1204–1225, 1981.

[136] S. Phipps, T.H.J. Yang, F.K. Habib, R.L. Reuben, and S.A. McNeill. Measurement of tissue mechanical characteristics to distinguish between benign and malignant prostatic disease. *Urology*, 66(2):447 – 450, 2005.

[137] D. Purves, G. J. Augustine, D. Fitzpatrick, W. C. Hall, A.-S. LaMantia, J. O. McNamara, and L. E. White. *Neuroscience.* Sianuer, Sunderland, MA:, 4th edition, 2008.

[138] HJ Qi, K. Joyce, and MC Boyce. Durometer hardness and the stress-strain behavior of elastomeric materials. *Rubber Chemistry and Technology*, 76:419–435, 2003.

[139] T. A. Quilliam. *Active Touch: The Mechanisms of Recognition of Objects by Manipulation*, chapter The structure of fingerprint skin, pages 1–18. Pergamon, London, U.K, 1978.

[140] E. M. Reimer and L. Danisch. Pressure sensor based on illumination of a deformable integrating cavity, 1999.

[141] LaMotte RH and Srinivasan MA. Tactile discrimination of shape: responses of slowly adapting mechanoreceptor afferents to a step stroked across the monkey fingerpad. *Journal of Neuroscience*, 7:1672–1681, 1987.

[142] S. L. Ricker and R. E. Ellis. 2-d finite element models of tactile sensors. In *IEEE Int. Conf. Robot. Autom.*, pages 941–947, Atlanta, GA, 1993.

[143] D. D. Rossi, G. Canepa, G. Magenes, F. Germagnoli, A. Caiti, and T. Parisini. kin-like tactile sensor arrays for contact stress field extraction. *Mater. Sci. Eng.*, C1:23–36, 1993.

[144] D. De Rossi and C. Domenici. Piezoelectric properties of dry human skin. *IEEE Trans. Electr. Insul.*, EI-21:511–517, 1986.

[145] J. Rossiter and T. Mukai. An led-based tactile sensor for multi-sensing over large areas. In *IEEE Sens.*, pages 835–838, Korea, 2006.

[146] R. A. Russell and S. Parkinson. Sensing surface shape by touch. In *IEEE Int. Conf. Robot. Autom.*, pages 423–428, Atlanta, GA, 1993.

[147] J. Scheibert, S. Leurent, A. Prevost, and G. Debregeas. The role of fingerprints in the coding of tactile information probed with a biomimetic sensor. *Science*, 323:1503–1506, 2009.

[148] P. A. Schmidt, E. Mael, and R. P. Wurtz. A sensor for dynamic tac- tile information with applications in human-robot interaction & object exploration. *Robot. Autonomous Syst.*, 54:1005–1014, 2006.

[149] Michael N. Shadlen and William T. Newsome. Neural basis of a perceptual decision in the parietal cortex (area lip) of the rhesus monkey. *Journal of Neurophysiology 86*, 4:1916–1936, 2001.

[150] M. Shikida, T. Shimizu, K. Sato, and K. Itoigawa. Active tactile sensor for detecting contact force and hardness of an object. *Sens. Actuators A*, 103:213–218, 2003.

[151] H. Shinoda, K. Matsumoto, and S. Ando. Tactile sensing based on acoustic resonance tensor cell. In *Solid State Sensors and Actuators, 1997. TRANSDUCERS '97 Chicago., 1997 International Conference on*, volume 1, pages 129 –132 vol.1, jun 1997.

[152] A. M. Smith, C. E. Chapman, M. Deslandes, J. S. Langlais, and M. P. Thibodeau. Role of friction and tangential force variation in the subjective scaling of tactile roughness. *Exp. Brain Res.*, 144:211–223, 2002.

[153] A. M. Smith, G. Gosselin, and B. Houde. Deployment of fingertip forces in tactile exploration. *Exp. Brain Res.*, 147:209–218, 2002.

[154] R.L. Smith and G.E. Sandland. An accurate method of determining the hardness of metals, with particular reference to those of a high degree of hardness. In *Proceedings of the Institution of Mechanical Engineers*, volume 1, pages 623–641, 1922.

[155] Smooth-On. Silicon rubber with shore 00 scale softness commercial website.

[156] Smooth-On. Silicon rubber with shore a scale softness commercial website.

[157] M. A. Srinivasan and R. H. LaMotte. Tactual discrimination of softness. *J. Neurophsiol.*, 73:88–101, 1995.

[158] J. C. Stevens and K. K. Choo. Temperature sensitivity of the body surface over the life span. *Somatosens. Motor Res.*, 15:13–28, 1998.

[159] A. Streri and Feron. The development of haptic abilities in very young infants: From perception to cognition. *Infant Behavior and Development*, 28:290–304, 2005.

[160] S. Takamuku, G. Gomez, K. Hosoda, and R. Pfeifer. Haptic discrimination of material properties by a robotic hand. In *Development and Learning, 2007. ICDL 2007. IEEE 6th International Conference on*, pages 1 –6, july 2007.

[161] E.L. Tobolski and A. Fee. Macroindentation hardness testing. *ASM Handbook*, 8:203–211, 2000.

[162] K Tomomatsu, 1977.

[163] Eduardo Torres-Jara, Iuliu Vasilescu, and Raul Coral. A soft touch: Compliant tactile sensors for sensitive manipulation. 2006.

[164] M. Tremblay and M. R. Cutkosky. Estimating friction using incipient slip sensing during a manipulation task. In *IEEE Int. Conf. Robot. Autom.*, pages 429–434, Atlanta, GA, 1993.

[165] A B Vallbo and R S Johansson. Properties of cutaneous mechanoreceptors in the human hand related to touch sensation. *Human Neurobiology*, 3(1):3–14, 1984.

[166] H. B. Wasling, U. Norrsell, K. Go thner, and H. Olausson. Tactile di- rectional sensitivity and postural control. *Exp. Brain Res.*, 166:147–156, 2005.

[167] Karsten Weiss and Heinz Woern. Tactile sensor system for an anthropomorphic robotic hand. *Control*, 7:587592, 2004.

[168] N. Wettels, V. J. Santos, R. S. Johansson, and L. G. E. Biomimetic tactile sensor array. *Adv. Robot.*, 22:829–849, 2008.

[169] J. M. Wolfe, K. R. Kluender, D. M. Levi, L. M. Bartoshuk, R. S. Herz, R. L. Klatzky, and S. J. Lederman. *Sensation and Perception.* Sunderland, 2006.

[170] M.R. Wolffenbuttel and P.P.L. Regtien. Polysilicon bridges for the realization of tactile sensors. *Sensors and Actuators A: Physical*, 26(13):257 – 264, 1991. ¡ce:title¿Proceedings of Eurosensors IV held in jointly with Sensoren Technologies und Anwendung¡/ce:title¿.

[171] R. J. Woodham. Gradient and curvature from photometric stereo including local confidence estimation. *Journal of the Optical Society of America A*, 11:3050–3068, 1994.

[172] D. Yamada, T. Maeno, and Y. Yamada. Artificial finger skin having ridges and distributed tactile sensors used for grasp force control. *J. Robot. Mechatron.*, 14(2):140–146, 2002.

[173] Yue Yang, Kazuo Yamazaki, Hideki Aoyama, and Sadayuki Matsumiya. Fiber optic surface topography measurement sensor and its design study. *Precision Engineering*, 24(1):32–40, 2000.

[174] J. Yuji and C. Sonoda. A pvdf tactile sensor for static contact force and contact temperature. In *IEEE Sens.*, pages 738–741, Korea, 2006.

[175] Hong Zhang and E. So. Hybrid resistive tactile sensing. *Systems, Man, and Cybernetics, Part B: Cybernetics, IEEE Transactions on*, 32(1):57 –65, feb 2002.

[176] Man Zhang, Priya Nigwekar, Benjamin Castaneda, Kenneth Hoyt, Jean V. Joseph, Anthony di Sant'Agnese, Edward M. Messing, John G. Strang, Deborah J. Rubens, and Kevin J. Parker. Quantitative characterization of viscoelastic properties of human prostate correlated with histology. *Ultrasound in Medicine & Biology*, 34(7):1033 – 1042, 2008.

[177] A. Bodega rd, A. Ledberg, S. Geyer, E. Naito, K. Zilles, and P. E. Roland. Object shape differences reflected by somatosensory cortical activation in huma,. *J. Neurosci.*, 20(RC51):1–5, 2000.